Optically Detected Magnetic Resonance: Computational Predictions and Experimental Results

Scott Leland Crossen

A senior thesis submitted to the faculty of
Brigham Young University
in partial fulfillment of the requirements for the degree of

Bachelor of Science

Dr. John S. Colton, Advisor

Department of Physics and Astronomy

Brigham Young University

April 2018

Copyright © 2018 Scott Leland Crossen

All Rights Reserved

ABSTRACT

Optically Detected Magnetic Resonance: Computational Predictions
and Experimental Results

Scott Leland Crossen
Department of Physics and Astronomy, BYU
Bachelor of Science

Electron spin resonance (ESR) is an important tool in understanding the quantum-mechanical properties of condensed matter. Its applications range from studying lattice defects in solids to studying spin coherence in qubit candidate materials used for quantum computing. When coupled with a photoluminescence measuring component, it is possible to optically record ESR information contained in the resulting induced light. This unique form of ESR is called optically detected magnetic resonance (ODMR). In this thesis we compare experimental ODMR data with ESR predictions generated from a computational modeling system. To investigate the differences between these two methods we will study one spin-system in particular: irradiated 4H silicon carbide. This specimen will serve as the primary means to connect the two very different forms of computational and practical ESR spectroscopy commonly used today. Methods and theory for both methods will be described and resulting spectra will be presented for comparison. Though there will always be some differences, results show that computational ESR predictions match experimental results to the same extent that the underlying Hamiltonian for that particular system is understood.

Keywords: [optically detected magnetic resonance, ODMR, Electron Spin Resonance, ESR, electron paramagnetic resonance, EPR, EasySpin]

ACKNOWLEDGMENTS

Undergraduate research with Dr. Colton was the single most valuable experience I had during my time at BYU. For this, I'd like to thank Dr. Colton for always being incredibly helpful and available whenever I needed assistance, and for being patient during the semesters when my class schedule prevented me from making more of a contribution to our work. Throughout both of my majors, I have never had a better professor in the classroom nor one that can present difficult concepts with as much clarity as he can.

I also couldn't have done this without the financial support from the Physics Department and BYU's Office of Research and Creative Activities.

My lab partners also deserve an acknowledgement. These include Jacob Embley, Kameron Hansen, and Ryan Peterson. Some of the experimental work was made possible by Dr. Sam Carter who was very helpful throughout this work.

I would also like to acknowledge the help, encouragement, and inspiration that I've received from my twin brother Mark Crossen, my parents and all of Brady Parks, Sydney MacFarlane, John Hancock, Doug Patterson, and Megan Parks.

For the reader: it was my intention to make this thesis succinct, brief, and tasteful in the content that it covers. I hope that I achieved my goal for your sake.

Contents

Table of Contents **iv**

List of Figures **1**

1 Introduction **3**
1.1 Qualitative Description of ESR and ODMR . . . 3
1.2 Electron Spin, Quantum Computing, and Qubits . . . 5
1.3 The Defect Nature of Materials . . . 7
1.4 Previous Work . . . 7
1.4.1 Preliminary Work and Results . . . 7
1.4.2 Experimental Setup . . . 8
1.4.3 Samples and Collaborative Efforts . . . 9
1.4.4 Preliminary Results of Experimental ODMR . . . 9
1.4.5 *EasySpin* Computational Modeling System . . . 10
1.5 Overview of Thesis . . . 11
1.6 Explanatory Notes and Background Information . . . 12

2 Computational Model and Theory **14**
2.1 Mathematical Theory . . . 14
2.2 *EasySpin* Interaction Modeling System . . . 16
2.2.1 The *EasySpin* Struct Definition . . . 16
2.2.2 Basic Class Structure . . . 17
2.3 Selecting Hamiltonian Arguments . . . 18
2.3.1 ZnO Nanowires . . . 19
2.3.2 Irradiated 4H-SiC . . . 21

3 Experimental Methods **24**
3.1 Sample Preparation . . . 24
3.1.1 Preparation of Silicon Carbide Samples . . . 24
3.1.2 Photoluminescence Data . . . 26
3.2 Experiment Background . . . 26
3.3 Experiment Setup . . . 27

3.3.1 Temperature Controller and Static Magnetic Field 27
3.3.2 Laser and Optics 28
3.3.3 Microwave Generation and Amplification 28
3.3.4 Software Controller Interfaces and Data Recording 29

4 Results **30**
4.1 Computational Predictions 30
4.2 Experimental Results 31
4.3 Data Analysis 33
4.4 Related Work 34
4.5 Conclusion 34

Appendix A Electron Spin Coherence of Silicon Vacancies in Proton-Irradiated 4H-SiC **36**

Appendix B Electron Spin Studies of Electron Irradiated SiC **45**

Appendix C Optical Studies of Cadmium Telluride **48**

Bibliography **50**

Index **53**

List of Figures

1.1 Zeeman Effect and Resonant Conditions in Matter 5

1.2 Preliminary ODMR Data 10

1.3 Magnetic Field and Microwave Frequency Relationship 11

2.1 Simple Spin System Definition 17

2.2 ESR Spectrum Presented by Stehr et al. 20

2.3 Recreation of ZnO Nanowire ESR 20

2.4 The *EasySpin* Representation of ZnO Nanowires 21

2.5 Energy Levels of 4H-SiC 22

2.6 The *EasySpin* Representation of SiC 22

3.1 SiC Depth-Dependent Photoluminescence 25

3.2 Photoluminence Spectra of Silicon Carbide 26

3.3 Diagram of Experimental Setup for ODMR 27

4.1 ESR Computational Model for SiC 31

4.2 Experimental ODMR for SiC 32

4.3 ESR Computational Model for SiC 32

B.1 Electron Irradiated SiC Temperature Dependence for Single-Exponential Spin Coherence 46
B.2 Electron Irradiated SiC Temperature Dependence for Single-Exponential Spin Coherence 46
B.3 Electron Irradiated SiC Temperature Dependence for Single-Exponential Spin Coherence 47

C.1 Photoluminesce spectrum for CdTe at 17.5 K 49
C.2 Photoluminesce spectrum for CdTe at room temperature 49

Chapter 1

Introduction

1.1 Qualitative Description of ESR and ODMR

Optically detected magnetic resonance (ODMR) is a particular form of *electron paramagnetic resonance* (EPR) which is more commonly known as *electron spin resonance* (ESR). The latter two of these terms (EPR and ESR) are synonymous; the former (ODMR) is a particular subset of ESR that utilizes an optical measuring technique as a means to collect ESR information. In literature, it is common to see both of these terms followed by the designation "spectroscopy" which signifies that they are tools to study properties of matter via electromagnetic radiation. Though the extent of their application has grown over the years, ESR and ODMR are most commonly used to study the spin properties of electrons and electron-holes trapped in crystal lattices. They can be used to study free radicals in organic materials [1] and are also important in studying the local environment of lattice defects through a technique using angular-dependent ODMR. One particular use of ODMR is the study of electron-spin coherence via a technique known as electron spin echo. This can be useful when studying what properties and conditions lead to superior state coherence for qubit candidate materials in quantum computing [2].

The intellectual foundation of electron spin resonance is rooted in quantum mechanics. Bound electrons in matter have discrete and quantized energy levels that govern what frequencies of light are emitted when transitions between energy levels are made. For electron systems, which are fermions and thus subject to the Pauli exclusion principle, the energy levels are two-level degenerate when bound in matter. In quantum mechanics we choose to describe this degeneracy in terms of spins: we say an electron is either "spin up" or "spin down". Each energy level can have at most two electrons of opposite spins inhabiting it (and thus the degeneracy). The spin terminology is used as to compare electrons to particles. It describes the principle of conservation of angular momentum that would be found in a classical system such as a top. In the case of an electron, the electron's spin is a description of the magnetic moment's alignment to an external magnetic field. For electrons bound in matter, the energy levels of the molecule will split in an applied magnetic field according to the Zeeman effect and the spin states of the electrons can be observed — often through a photoluminescence or other fluorescence measuring technique such as what we will use here.

The Zeeman effect itself is crucial in understanding the principles of ESR. In the presence of a magnetic field, populations of free electrons will form a spin-1/2 system between a lower-energy "spin-up" state and a higher-energy "spin-down" state. In matter, different half-integer values of spin states can be formed between the interactions of different energy levels with different transition selection rules. A spin-1/2 system in the presence of a magnetic field is shown in Figure 1.1. As seen here, the energy levels of the two differing spins diverge linearly for an increasing magnetic field. The difference in energy between these two levels is typically in the microwave frequency domain (for field magnitudes of a few tesla). For higher spin-parity systems, a given magnetic-field strength will result in a set of characteristic microwave frequencies that the electrons are most prone to emit when transitioning between quantized states. In a spin-1/2 system there will only be one frequency corresponding to the difference between the two Zeeman lines at the given

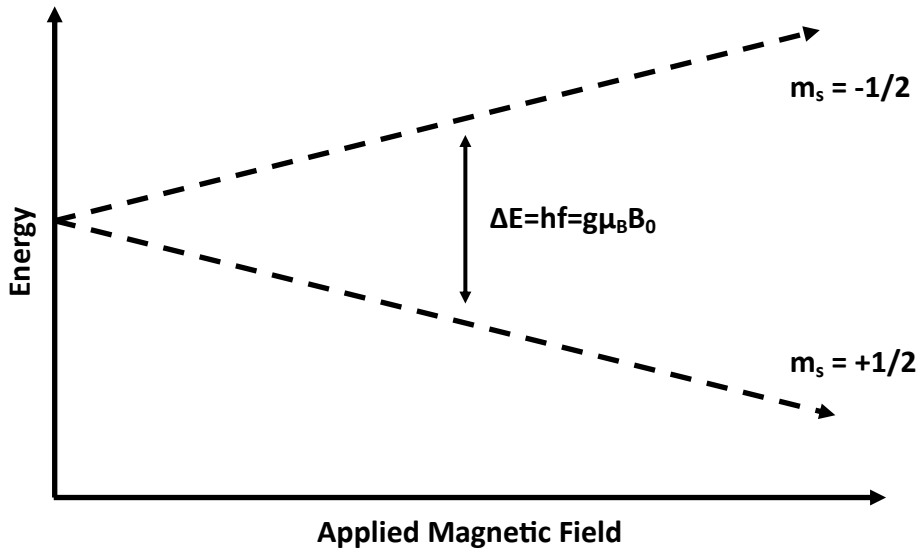

Figure 1.1 Zeeman effect for a two level system showing spin ($\pm 1/2$) energy levels as a function of applied magnetic field. For arbitrary field strength the energy difference is shown as a function of μ, g, and the field strength B_0.

field strength. Likewise, for a given microwave frequency, there will be a variety of magnetic field strengths which are able to transition bound electrons between states. This unique pairing between both the microwave frequency and magnetic field strength is the resonant condition upon which ESR is based on and also the means it uses to discover information about materials.

1.2 Electron Spin, Quantum Computing, and Qubits

Classical computation is based upon a binary system where the computer's register, memory, and general logical states are either in logical "true" or logical "false" states. A "true" state usually corresponds to a high voltage and a "false" state usually corresponds to a grounded voltage. A computer's bits can be in either of these two states — 1 or 0 — but not both.

A spin-1/2 system also describes a binary system between a higher energy basis state and a lower energy basis state. In this comparison, the spin-1/2 system will be measured (and the wave

function collapsed) to be in either of these two states — but not both. One important difference between the the spin-1/2 system and the classical computer bit model is that the spin system can have states that exist as a linear combination of the two basis up/down states. In accordance with quantum mechanics, this means that the spin-1/2 system can exist as a superposition between both the spin up and spin down states and has a certain probability of being measured in each. It is important to note that this superposition does not mean that the state exists as some value between an excited state and a lower state. Rather, it exists with some value in both states simultaneously.

Because of this unique property of spin systems, they can be used as a basis for forming what is called a "quantum computer" [3]. Though it largely depends on the architecture, quantum computers can be considered to manipulate information in a similar fashion to that of classical computers. Both have logical operators and storage bits and both are algorithmically based. Quantum computers, however, utilize this unique possibility of superposition and entanglement between states to make probabilistic calculations for many different states at the same time. This happens through quantum mechanical operations that initialize and manipulate states stored in "qubits" — the quantum computer's version of classical bits that can exist in superposition types of states.

Today, there is large emphasis within the scientific community in building viable, scalable quantum computers. The reason for this is that quantum computers offer reduced computational times for certain types of algorithms. Important to note, however, is that these machines are not necessarily more adept at common tasks, but are rather designed to carry out a few types of intense calculations in times logarithmically dependent on input for problems that would normally have a polynomial time dependence. The most notable use for quantum computers in our modern society is within the field of computer security and encryption. Quantum computers have the ability to compute prime factors via Shor's algorithm in a much faster time than traditional computers [4]. This ability would essentially render all of the current RSA encryption methods obsolete along with everything else that relies on public/private key encryption such as bitcoin.

Although more than just spin systems can be used as the all-important qubits for quantum computing, we will focus on this type — specifically spin-1/2 systems formed from electrons — for the basis of our discussion [5]. As mentioned earlier, ESR is the major tool used to study the spin properties of materials. In the case of quantum computation, ESR is used to study possible qubit materials that might eventually be used in such machines. Currently, one of the major difficulties in creating quantum computers is finding materials that can form superposition states that remain coherent (and reliable) over prolonged periods of time. In order to understand what properties of materials lead to superior qubit construction and state coherence, ESR can be used in conjunction with electron spin echo experiments to study the coherence of electrons in a spin-1/2 system. Moreover, ESR can be used alone to study the spin system itself and the local environment of the defects in materials that form them. Knowledge of this important topic will serve to increase our ability to construct better qubits for use in quantum computers.

1.3 The Defect Nature of Materials

In solid-state physics, materials form crystal lattices. These structures are not perfect, however, and often have intrinsic point defects [6]. These defects are important as they contribute to the overall spin system of the material via either electrons or holes [7]. For some materials, these defects can be introduced via high fluence irradiation of particles such as SiC which we will study.

1.4 Previous Work

1.4.1 Preliminary Work and Results

The work performed in this thesis references in large part the work done by Kyle Miller and Jacob Embley, two students who worked under Dr. John Colton and have since graduated from Brigham

Young University. Their work was mostly performed on the topic of electron spin coherence in proton-irradiated silicon carbide and is documented in their senior theses, both of related titles [8] [9]. This thesis, however, will not be on the same topic as the former two but will expand on one aspect used by both of these two students in their work, ODMR. In addition, both Miller and Embley used a particular species of 4H-SiC which is one of the two principal materials of investigation in this thesis.

Appendix A includes a publication that Embley, Colton, Miller, myself and a few others produced on the topic of spin coherence in proton irradiated silicon carbide [10]. It has been accepted by *Physical Review B* and appeared in publication during the year 2017. This publication serves as a capstone to the work of both Embley and Miller as included in their senior theses and will serve as the context for which this thesis was produced.

In addition to the work done by Miller and Embley, an additional study was performed on a similar material of the SiC specimen which is not included in either the aforementioned theses or publication. The major difference with this project and the theses produced by Miller and Embley is the type of irradiation used on the SiC sample in question. Miller's work was primarily concerned with a 10^{14} cm^{-2} proton-irradiated sample of SiC. Embley likewise worked with a 10^{13} cm^{-2} proton-irradiated sample of SiC. In that project I worked with a 10^{17} cm^{-2} electron-irradiated sample of SiC in much the same way as used by Embley. With this additional sample, a more comprehensive analysis and additional results are presented.

1.4.2 Experimental Setup

The experimental setup used for the majority of this thesis was set up and tested by Kyle Miller and Jacob Embley. Miller initially set up all the necessary instrumentation to be used in his experiment which is detailed in his thesis. Later, Embley improved upon most of Miller's design and achieved increased precision and improved results [9]. The experiment used by both Embley and Miller

was eventually repurposed and slightly modified for the experiment detailed in this thesis. A full summary and implementation of the experimental setup can be found in section 3.3. This section includes both the setup used by Miller and Embley as well as the components I modified for the purposes of performing this work.

1.4.3 Samples and Collaborative Efforts

The work done for this thesis was done in collaboration with Dr. Sam Carter of the Naval Research Lab. Ultimately, Dr. Carter was responsible for producing and partially characterizing the silicon carbide used in our experiments [11]. These samples were irradiated with different fluences of particles in order to introduce different concentrations of defects into the material. It was Carter's work that ultimately led us to obtain such high quality samples for optical characterization and electron spin resonance studies.

1.4.4 Preliminary Results of Experimental ODMR

This thesis is based around one primary material, SiC, which was previously characterized for ODMR.

Dr. Sam Carter of the Naval Research Lab provided the SiC samples we used. According to his characterization, the silicon vacancies in silicon carbide form a spin-3/2. This system also has a zero-field splitting effect which creates an energy difference between the positive and negative spin states even with no external field (+3/2, +1/2 with -3/2, -1/2).

In addition Dr. Carter also provided preliminary ODMR results performed at low field strengths of around 31 mT [11]. The results of his measurements are found in Figure 1.2 and show the transitions between different spin states which will be more fully developed in section 3.1.1. Moreover, Carter also provided angular dependent measurements of resonant conditions between magnetic field strength and microwave frequency. As mentioned in section 1.1, for a given magnetic field

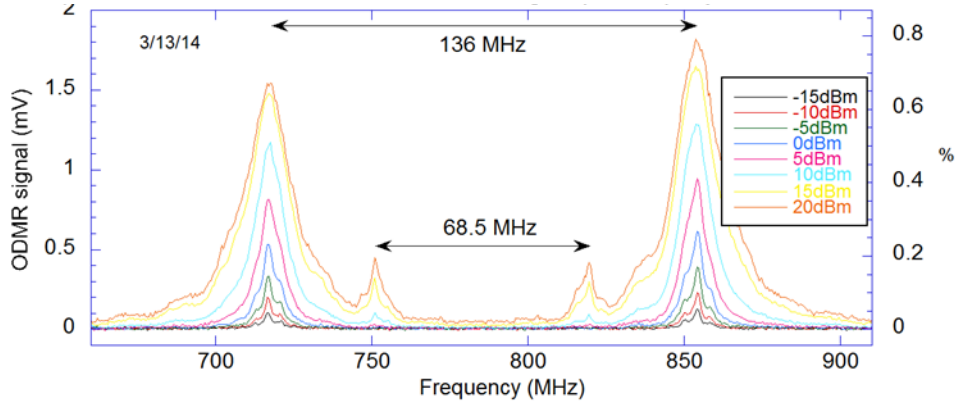

Figure 1.2 The preliminary ODMR data for proton irradiated silicon carbide in a constant magnetic field of 28 mT. The plot shows resonant paramagnetic conditions at 718 MHz and 857 MHz where the absorption is greatest.

strength there will exist different resonant frequencies depending on the spin system in question. In addition, these characteristic frequencies will have associated linewidths that describe what range of frequencies the resonance is centered around and how wide it is. For the case of a spin-3/2 system as found in 4H-SiC, the relationship is best represented by Figure 1.3 which is a plot produced by Dr. Carter for the samples used in this project [11].

1.4.5 *EasySpin* Computational Modeling System

EasySpin [13] is a library for MATLAB designed to computationally model ESR data. The majority of computational work for this thesis was done using this program which was provided free of charge through the program's website. Though most of the necessary functions to model ESR data were included in the *EasySpin* library, I still found it necessary to create custom definitions in addition to what was already supplied.

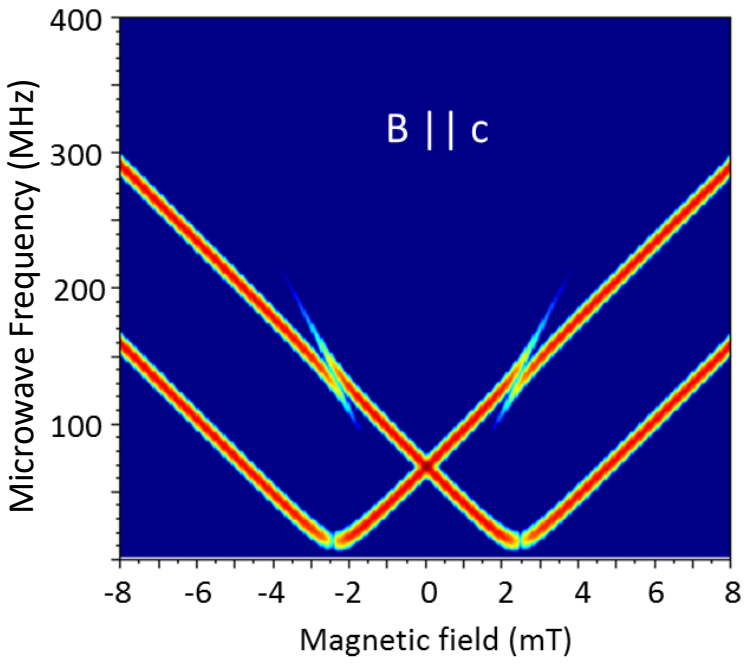

Figure 1.3 The relationship between magnetic field strength and microwave frequency for 4H-SiC, a spin-3/2 system. Color Brightness indicate resonant conditions. Notice the linear dependence between both microwave energy and field strength. From Ref. 12.

1.5 Overview of Thesis

The purpose of this thesis is to describe in detail the methods and procedures behind experimental and theoretical ESR and to answer the question as to how both experimental and theoretical methods compare to each other. By so doing we will also introduce the fundamental theory behind ESR and computational modeling packages such as *EasySpin*. In addition, we will also discuss the experimental frameworks and setups necessary for collecting ODMR information from materials. This analysis will not be comprehensive but is rather purposed as an introduction into the techniques used in the field. As such, we will restrict our analysis to only solid-state ESR and ODMR.

We will use one main material for this thesis: SiC. This material will be valuable in our understanding of lattice defect contribution towards ODMR results. In addition, we will primarily

use this material as a control to compare the experimental data with respective computational predictions. It will be through this material that we will ultimately show the similarity between experimental results and theoretical predictions.

In the end, this thesis will conclude that computational modeling is accurate to the same degree the spin system is understood. In other words: the level of precision that computational modeling can present is restricted by how much information is known about the Hamiltonian for that given system.

1.6 Explanatory Notes and Background Information

The content of this thesis will use the term *ESR* when referring to the general theory and mathematical model of electron spin resonance and will use the term *ODMR* when referring to the experimental methods used for collecting ESR information. As mentioned earlier, ODMR is a specific type of ESR that is ultimately used to collect the same information through a fluorescence technique. Because we have implemented an ODMR-type experiment in our lab we will use this term for descriptive accuracy when referring to our experimental application.

By way of information, the work done for this thesis was performed using MATLAB R2016b (version 9.1) and *EasySpin* version 5.1.9 . It will be assumed that the reader is proficient in basic MATLAB or C constructs and is at least familiar with data types and terms such as "struct", "parameter" and "field" as related to computer programming.

All plots and figures were created using a combination of Mathematica version 10.4 and Origin version 7.5.

In addition, pertinent git repositories will be hosted online via GitHub for all code developed for this project. The LabVIEW suite used for data acquisition can be found at the permanent URL https://github.com/coltonlab/LabVIEW-programs. The programs developed on top of the

EasySpin library that were used for theoretical modeling can be found along with this thesis at https://github.com/scottcrossen/SeniorThesis.

Chapter 2

Computational Model and Theory

2.1 Mathematical Theory

As mentioned in the Introduction, spin systems and electron spin resonance (ESR) are best understood in terms of interaction Hamiltonians. "Hamiltonians" in this context are quantum mechanical operators that act on energy states and form specific eigensystems with defined energy eigenvalues. For example, in the Zeeman effect there exists a Hamiltonian that when diagonalized gives the energy-splitting for a given magnetic field in terms of its eigensystem. Since ESR spectroscopy measures the resonant conditions between energy-levels and magnetic field strength, it is necessary to calculate the field-dependent Hamiltonian for each system before we can calculate the theoretical ESR spectrum.

Thankfully, the general Hamiltonian for atoms in a magnetic field is commonly known. In this case, the interaction energy of an atom in a constant magnetic field is given by the overall spin Hamiltonian $\mathscr{H}_{\text{tot}}$ [14]

$$\mathscr{H}_{\text{tot}} = \mathscr{H}_{\text{elect}} + \mathscr{H}_{\text{cf}} + \mathscr{H}_{\text{LS}} + \mathscr{H}_{\text{SS}} + \mathscr{H}_{\text{Zee}} + \mathscr{H}_{\text{hfs}} + \mathscr{H}_{\text{Q}} + \mathscr{H}_{\text{N}}$$

where $\mathscr{H}_{\text{elect}}$ is the electronic energy, $\mathscr{H}_{\text{cf}}$ is the crystal field energy, $\mathscr{H}_{\text{LS}} = \lambda \mathbf{L} \cdot \mathbf{S}$ is the spin-

orbit interaction, $\mathscr{H}_{\mathrm{SS}} = D\left[S_z^2 - \frac{1}{3}S(S+1)\right]$ is the spin-spin interaction, $\mathscr{H}_{\mathrm{Zee}} = \beta\mathbf{H}\cdot(\mathbf{L}+\mathbf{S})$ is the Zeeman interaction energy, $\mathscr{H}_{\mathrm{hfs}} = (A_xS_xI_x + A_yS_yI_y + A_zS_zI_z)$ is the hyperfine structure, $\mathscr{H}_{\mathrm{Q}}$ is the quadrupole energy, and $\mathscr{H}_{\mathrm{N}} = \gamma\beta_N\mathbf{H}\cdot\mathbf{I}$ is the nuclear spin energy. All of these components are defined in terms of the magnetic field $\mathbf{H}$, the spin angular momentum operator $\mathbf{S}$, the orbital angular momentum operator $\mathbf{L}$, the nuclear spin operator $\mathbf{I}$, the Bohr magneton β, the spin-orbit coupling constant λ, the hyperfine coupling constant A, the nuclear gyromagnetic ratio γ, and the zero-field splitting constant D.

Some terms in the Hamiltonian dominate the system and can be focused on individually. The most important term is the Zeeman interaction energy. For the high-field limit that we will be working with, the Zeeman interaction dominates all other perturbations. This affects the system by splitting energy levels linearly with increasing magnetic field. Though there are a few other constants involved in the calculation of the Zeeman Hamiltonian, the main parameter it requires is the all-important g-tensor which can be extracted from the Hamiltonian given above. We can show this process explicitly by writing the form of the Zeeman interaction as $\mathscr{H}_{\mathrm{Zee}} = \beta\mathbf{H}\cdot(\mathbf{L}+\mathbf{S})$. Simplifying this for a constant field in one direction gives $\mathscr{H}_{\mathrm{Zee}} = \frac{\mu_B\mathbf{B}}{\hbar}\cdot(g_lL_z + g_eS_z)$ where g_l is the gyromagnetic ratio corresponding to the orbital angular momentum and g_e is the gyromagnetic ratio corresponding to the spin angular momentum. Now if we solve specifically for the Zeeman corrections to individual terms ΔE_{Zee} we get $\Delta E_{Zee} = \frac{\mu_B\mathbf{B}}{\hbar}\cdot(g_lm_l\hbar + g_em_s\hbar)$ where m_l and m_s are orbital and spin quantum numbers respectively. In the coupled basis we typically represent this in terms of one g-factor g and one quantum-number m: $\Delta E_{Zee} = g\mu_B\mathbf{B}m$. The resulting g-tensor is specific to individual materials and simplifies to a single value for symmetric lattice conditions. It describes the spreading of the different spin energy levels in the magnetic field and it is ultimately through this Zeeman effect that we are able to see resonant conditions between magnetic field strength and microwave frequency.

Once the Hamiltonian is known for the system, the ESR spectrum can be computationally

predicted. A variety of methods are available to go from the basic Hamiltonian components to the finished ESR plot. The most notable is a software suite called *EasySpin* [15], which vastly simplifies the amount of calculations and explicit Hamiltonian definitions that the investigator has to make.

2.2 *EasySpin* Interaction Modeling System

The purpose of this thesis is to show the unique methodologies of both computational and experimental ESR. As for the former of these two, the most common tool used to computationally model ESR is known as *EasySpin* [15]. This package is built as an open library on top of the MATLAB program and serves to add functionality to the already-useful suite of functions that components within MATLAB.

2.2.1 The *EasySpin* Struct Definition

The core utility of the *EasySpin* package is the definition used in the spin system. The *EasySpin* library is built around the idea of a struct (a term describing a publicly-scoped group of fields) to define all necessary components of the system being studied. In fact, most methods in the *EasySpin* library usually require just a struct of this type as the sole parameter in the function declaration.

The struct represents the spin system and is usually defined by the user to the extent that the system is known. Though there are many optional parameters that can be included in the struct, the most rudimentary spin system needs to include a "sys.S" parameter representing either a list or a value for the half-integer value of spin being worked with as well as a "sys.g" parameter to represent the g-factor of that material in solid-state ESR. The g-factor could be either a list or a single value depending on the crystal type being investigated. After these two parameters are defined, the system can then be passed to any other functions for analysis and plotting. Figure 2.1

```
Sys.S = 1/2;
Sys.g = 2.017;
Sys.lw = 1;

Exp.mwFreq = 9.2;  % GHz
Exp.Range = [320 330]; % mT
```

Figure 2.1 An example declaration of the basic *EasySpin* struct used in defining the spin system. In this example, "Sys" represents an arbitrary name for the struct, "sys.S" is the spin parity, "sys.g" is the g-factor, 'sys.lw' is the ESR line-width, "sys.mwFreq" is the position of the microwave frequency being probed, and "sys.Range" is the range of the magnetic field being scanned.

shows an example of what this basic definition might look like in MATLAB.

2.2.2 Basic Class Structure

The term "class" is used loosely in this context. Unlike most languages, MATLAB (and thus *EasySpin*) is based on plain C and is thus not really object oriented. However, unlike C, basic class definitions have been added to MATLAB though they aren't commonly used. *EasySpin* uses a series of "sys.m" files that represent different abstractions of the overall modeling system that may or may not be implemented in the form of classes. For this thesis, I will use the term "class" to refer to any modular component of the provided *EasySpin* library.

The most notable classes that are supplied with the library are the core plotting functions for ESR spectra [16]. These include such names as "garlic" for cw isotropic ESR and "pepper" for solid state CW ESR (which I will use). Table 2.1 shows the full list of possible plotting functions supplied in the library. Other functions supplied in *Easyspin* are mostly related to data import/export, data analysis, and system optimization.

Table 2.1 List of possible *EasySpin* plotting functions. '*pepper*' is the main function that will be used in this thesis.

Function	Description
garlic	cw EPR, isotropic and fast motion
chili	cw EPR, slow motion
pepper	cw EPR, solid state
salt	ENDOR, solid state
saffron	pulse EPR/ENDOR, solid state
curry	SQUID magnetometry
blochsteady	Bloch equations, steady-state
pulse	Shaped pulses
esfit	least-squares fitting

In addition to the classes supplied in the *EasySpin* library, I have also built a few of my own for better visualization of spin systems. One such class (which is included in the online repository cited in the introduction) is called "zeeman.m". This program plots the field splitting of the Zeeman interactions in the spin system vs increasing magnetic field. Another class I implemented builds upon this one and is called "animate.m". This plots the Zeeman diagram and then animates the plot by drawing the resonant magnetic field differences for a given microwave frequency. Again, all of these additional classes are included in an online repository linked to in the introduction of this thesis.

2.3 Selecting Hamiltonian Arguments

In order to imitate the ESR spectrum via *EasySpin*, the Hamiltonian for the materials needs to be understood to the fullest possible extent.

2.3.1 ZnO Nanowires

As a demonstration of how to use *EasySpin*, I have recreated the results given by J. E. Stehr in his publication regarding the resonant properties of zinc oxide nanowires [17]. In this paper, the author Stehr models the ESR spectrum using g-tensor and spin-values given for each defect center of ZnO nanowires. This data is summarized in Table 2.2. Stehr used the *EasySpin* modeling system to show the predicted ESR spectrum resulting from the V_{Zn}^{-}, V_{Zn}/Zn_i, and D^* defect center contributions. He modeled each Hamiltonian separately using *EasySpin* and then combined the results with MATLAB. Figure 2.2 shows the published plots.

Table 2.2 Summary of the spin Hamiltonian parameters for the various defect centers of ZnO nanowires given by J. E. Stehr et al [17]. The spin-parity and diagonalized g-tensor values are given for each defect center. For the non-axial centers, φ is the angle between the z and c axis.

		Axial		Nonaxial			
Center	S	$g_\perp$	$g_\parallel$	g_{xx}	g_{yy}	g_{zz}	φ (deg)
V_{Zn}^{-}	$1/2$	2.0193	2.0024	2.0173	2.0183	2.0028	110.75
Z	$1/2$	2.006	2.020				20
V_{Zn}/Zn_i	1			1.9888	1.9893	1.9815	110.75
Zn_i^{+}	$1/2$	1.9595	1.9605				0
D^*	$1/2$	1.9605	1.9565				0

However, one thing Stehr did not include was the ESR line-width parameters and derivations he used when constructing the spin system via EasySpin. As a verification for the process he used, I have included a reconstruction of the same ESR spectrum that was included in his publication. Through comparison I found that the line-width parameters used by Stehr were 1, 5, and 2 mT for V_{Zn}^{-}, V_{Zn}/Zn_i, and D^* respectively. Though it is unknown as to how he arrived at these values, it is likely that he compared the theoretical model to the experimental data until a reasonable fit was

achieved. In Figure 2.3 and 2.4 I give the re-creation of the spectrum and the code used to generate the spin system that Stehr used [17].

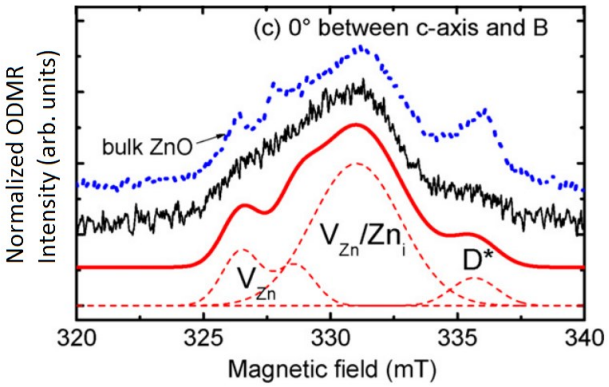

Figure 2.2 The ESR spectrum presented by Stehr et al for ZnO nanowires. The results of computational modeling using *EasySpin* are shown in dashed-red (individual) and solid-red (total). The black line represents actual data from the sample and the blue line is included for comparison to the bulk species. From Ref. 17.

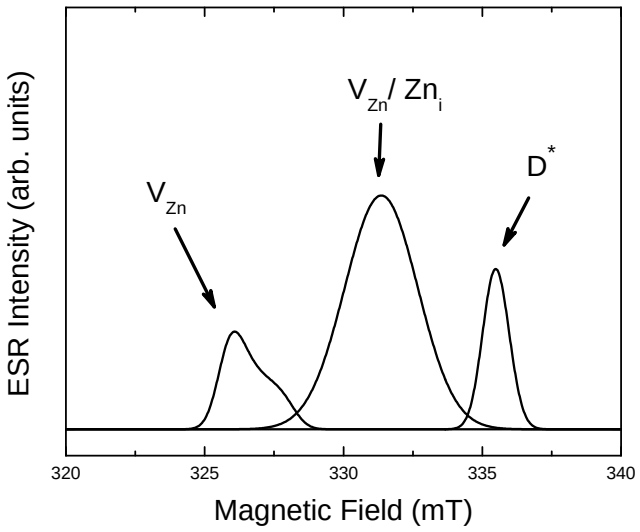

Figure 2.3 The re-creation of the plots given by Stehr et al. for the ZnO nanowire ESR spectrum. All three defect centers are included as in the original figure.

```
Sys1.S = 1/2;
Sys1.g = [2.0173, 2.0183, 2.0028];
Sys1.gFrame=[0 0 110.75];
Sys1.lw = 1;

Sys2.S = 1/2;
Sys2.gFrame=[0 0 20];
Sys2.g = [2.006 2.020];

Sys3.S = 1;
Sys3.g = [1.988, 1.9815, 1.9815];
Sys3.gFrame=[0 0 110.75];
Sys3.lw = 3;

Sys4.S = 1/2;
Sys4.g = [1.9595 1.9605];

Sys5.S = 1/2;
Sys5.g = [1.9605 1.9565];
Sys5.lw = 1;

Exp.mwFreq = 9.2;  % GHz
Exp.Range = [320 340]; % mT
Exp.Harmonic=0;
```

Figure 2.4 The *EasySpin* struct definition used in the re-creation of the plots given by Stehr et al.

2.3.2 Irradiated 4H-SiC

In order to computationally model the ESR spectrum for SiC, we first need to first construct the Hamiltonian for the system. In the following paragraphs I will detail the major components that make up the spin Hamiltonian for SiC. I have also included the pertinent code to represent this system in terms of the *EasySpin* struct definition in Figure 2.6.

SiC is commonly known to be a spin-3/2 system with two major ESR peaks in its spectrum [11]. The parameter "sys.S" given for the *EasySpin* system is simply $3/2$. Moreover, as mentioned previously, SiC has one major defect of interest: the silicon vacancy [18] [19] in its lattice structure. The g-factor for this defect is given as a rhomboidal two-termed g-factor (where $g_{xx} = g_{yy}$) where g_{zz} is almost exactly 2 [11]. This is listed as the "sys.g" parameter in the struct definition. The other term in the g-factor doesn't need to be included because we are using a normal crystal orientation.

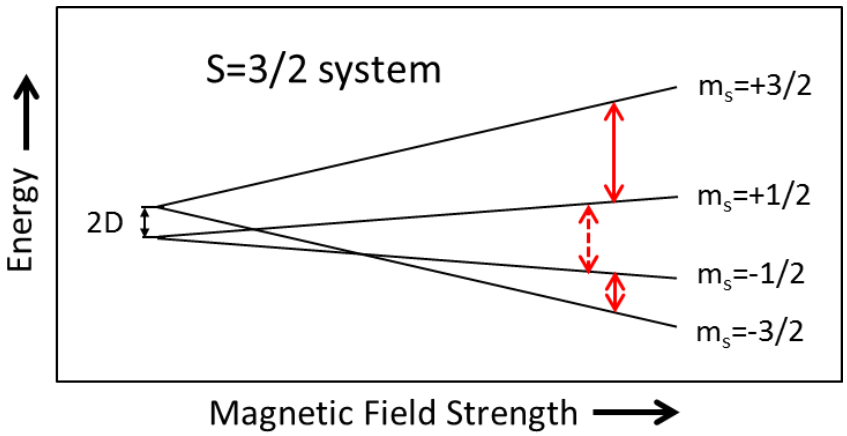

Figure 2.5 A diagram showing the energy-levels of the spin-3/2 system inherent in 4H-SiC for the high-field limit. Allowed transitions are shown with solid colored arrows. Disallowed transitions are shown with dashed arrows

```
Sys.S = 3/2;
Sys.g = 2.008;
%Sys.A = ??;
%Sys.Nucs = '29Si';
Sys.D = 34;
Sys.lwpp = [8 1];
Sys.DStrain=5;

Exp.Field = 370.78; % mT
Exp.mwRange=[10.2 10.6]; % GHz
Exp.nPoints=1024;
Exp.Harmonic=0;
Exp.Temperature=298;
Exp.CrystalOrientation = [0 0 0]*pi/180;

Opt.Transitions=[1 2; 3 4];
```

Figure 2.6 The representation of the known parameters included in the *EasySpin* struct definition for analysis of 4H-SiC

The linewidths are relatively narrow for specimens related to SiC. By comparison to experiment we have found that the full-width-half-maximum value of the line-widths is close to unity. Using *EasySpin* this means that the "sys.lw" parameter should be set to around 1. For the code provided in Figure 2.6 I have used a more-advanced form of Lorentzian line-broadening denoted as "sys.lwpp" to achieve this result. The difference is that "sys.lw" uses full-width-half-max width values and "sys.lwpp" uses peak-to-peak widths.

One interesting property of this material is that it exhibits a zero-field splitting which divides the $+3/2$ and $+1/2$ from the $-1/2$ and $-3/2$ states even when there is no external magnetic field. Our collaborater Dr. Sam Carter measured this parameter to be on the order of D = 70 MHz at the zero-field marking [11]. For the struct definition in Figure 2.6 we have used half of this value in accordance with the different definition of the term as used by *EasySpin*.

Moreover, only certain transitions are allowed in the SiC spin-3/2 system. Though other transitions can happen, they are unlikely and also undetectable because of the mechanism used by ODMR. For SiC the allowed transitions are between the energy levels of +3/2 to +1/2 and -3/2 to -1/2 [11]. To account for this effect in our *EasySpin* code we will use an optional parameter called "sys.Transitions" which we will set to only allow those transitions.

Though it is not readily apparent, SiC also exhibits hyperfine splitting in its major ESR peaks. To observe this splitting, two terms can be added to the spin-system: "sys.A" and "sys.Nucs". Unfortunately, the value of "sys.A" is not completely understood for the SiC system. In Figure 2.6 I have commented out two lines of code to reflect this fact.

Chapter 3

Experimental Methods

The work done for this thesis uses both computational and experimental components in describing ESR. We have described the process of theoretical/computational ESR in the last chapter. In this chapter we will describe the experimental methods of ESR which we call ODMR due to its optical-coupling of information gathering. This chapter is primarily concerned with detailing the experimental methods implemented in typical ODMR setups. We will first begin with a qualitative description of the material we studied (SiC).

3.1 Sample Preparation

3.1.1 Preparation of Silicon Carbide Samples

Three different samples of 4H-SiC were provided to us by our collaborator Dr. Sam Carter of the Naval Research lab. Each sample was prepared with a different irradiation fluence to introduce silicon defects into the lattice. The first sample that we tested was irradiated with 2 MeV protons at a fluence of 10^{14} cm^{-2}. The second sample was similarly irradiated with 2 MeV protons but at a fluence of 10^{12} cm^{-2}. The final sample was an electron-irradiated sample produced with a

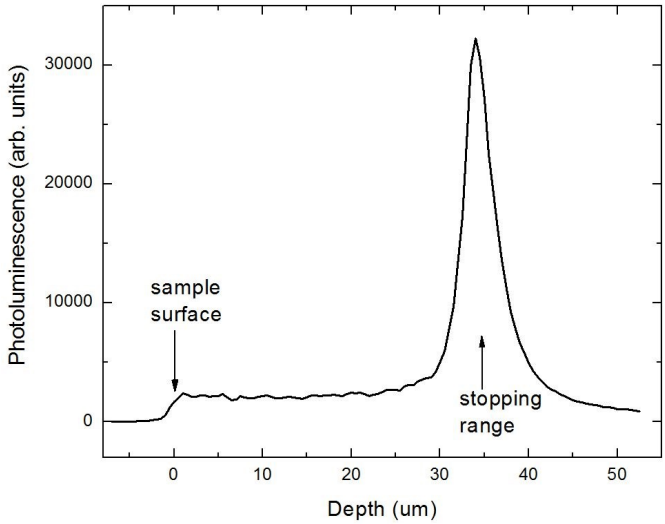

Figure 3.1 Depth-dependent photoluminescence of the 10^{12} cm^2 sample at at major PL peak taken at 25 K. The large peak at 34 μm indicates the stopping position of the protons. The spatial resolution was 1 μm. From Ref. 10.

fluence of 10^{17} cm^{-2}. The different strengths of irradiation in each sample is presumed to change the concentration of vacancy defects formed within the sample.

A higher irradiation fluence typically produces a higher concentration of defects. Figure 3.1 shows the depth stopping depth of irradiated protons in a 10^{12} cm^{-2} sample given to us by our collaborator Dr. Sam Carter. This plot of stopping depth should roughly correspond to the location of defects in the sample. From the stopping and range of ions in matter (SRIM) calculations, Dr. Carter predicted that the stopping distance of the ions would be at about 44 μm from the sample's surface. However, further photoluminescence studies showed the concentrations to be closer to about 32 μm rather than 44 μm.

Though we recorded the ODMR spectra for all the SiC samples, there was no real difference between any of them. By way of information, however, the data reported in this thesis corresponds to the the10^{12} cm^{-2} proton irradiated sample

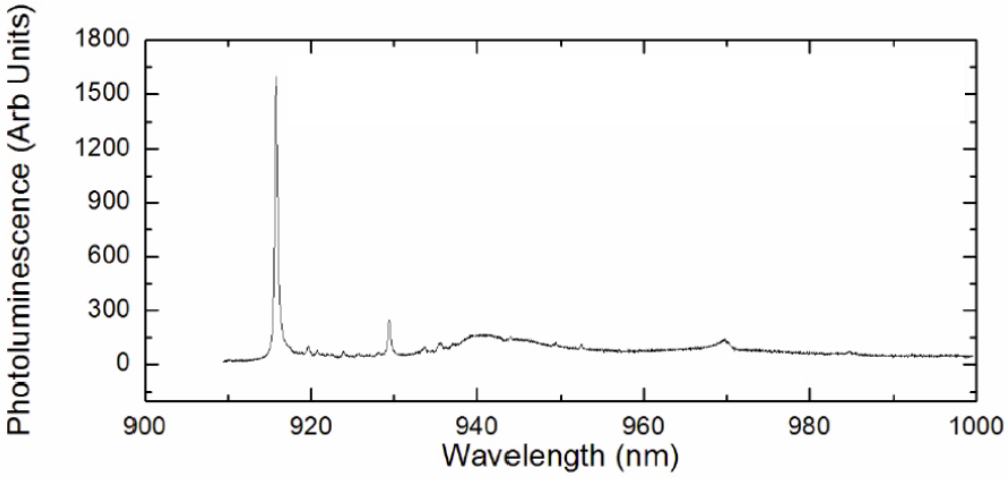

Figure 3.2 Photoluminence plot showing PL strength vs. wavelength in SiC taken at 6 K. The peak near 915 nm is the primary peak of interest as it represents the V2 silicon vacancy defect.

3.1.2 Photoluminescence Data

As mentioned earlier, ODMR is a particular type of ESR. The major difference is that ODMR uses a technique combining the resonant effects from ESR with the optical methods of photoluminescence to collect ESR data. Because of this, materials used with ODMR must have specific qualities in order for the absorption of the microwave frequencies to be measured by our detectors. Figure 3.2 shows the photoluminescence spectra of SiC with the major peak of interest shown at 917 nm.

3.2 Experiment Background

The experiments performed in this thesis were performed in tandem with another study involving electron spin coherence in silicon carbide. The majority of the equipment used in the spin-studies project was also used directly for collecting data for this thesis. Because of this, Section 3.3 only summarizes the more important elements and also those aspects of the experiment that significantly

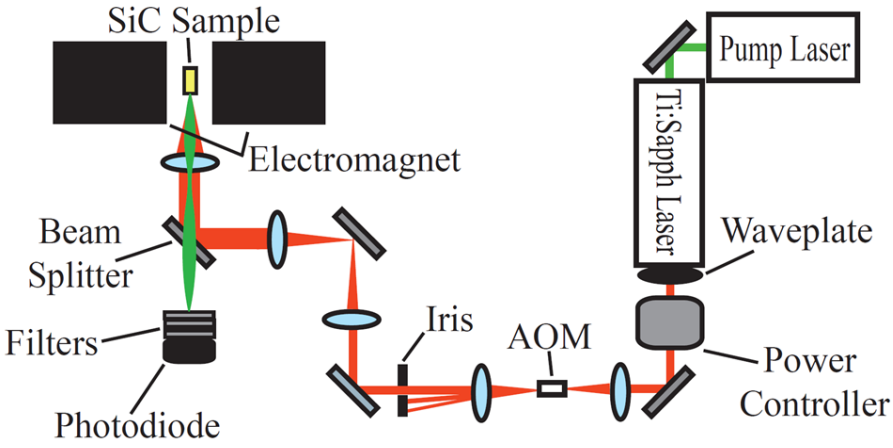

Figure 3.3 The diagram showing the necessary (labeled) components and arrangement for the ODMR experiment. A full description of each element is included in section 3.3.

deviate from previous projects. For a more detailed description of the experiment please reference Jacob Embley's undergraduate senior thesis. [9]

3.3 Experiment Setup

The overall setup used in this experiment is shown in Figure 3.3. The basic components necessary to collect ODMR data are: a laser to stimulate photoluminescence, a constant magnetic field, and a frequency-adjustable microwave generator to transition spins between energy levels. For our purposes the sample was mounted in a cryostat which kept it at a constant temperature for consistency in the experiment. These components are described in detail in the next section.

3.3.1 Temperature Controller and Static Magnetic Field

All samples that we studied were held at constant temperature and magnetic field. A nonmagnetic CryoIndustries cryostat was used to maintain constant temperature on the sample throughout the duration of the experiments. A turbopump was used in addition to the cryostat to keep the pressure around 10^{-5} mbar. A PID CryoCon controller was used as the heating element in the chamber.

When used in combination with the cryostat, any temperature between 8 K and 300 K could be achieved. Many different temperatures of ODMR were recorded for the samples between these two temperatures.

Most ESR-type experiments hold microwave frequency constant and sweep magnetic field strength, but for our purposes it was easier to do this in the reverse manner. As our data shows, the results can be interpreted the same way for either method. An external static magnetic field of 0.37 T was applied constantly throughout the experiment. A large iron-core electromagnet was powered using a Magna-Power Electronics TS Series IV power supply. A Lakeshore DSP 750 gaussmeter was used as a PID controller to make fine adjustments to the magnetic field so that it stayed constant at 0.37 T.

3.3.2 Laser and Optics

In order for photoluminescence to be measured off the sample, a laser was used to stimulate emission in the sample. The laser used for this experiment was a 3900 S Ti:Sapph laser tuned to 870 nm and pumped by a 532 nm solid diode laser. The Ti:Sapph was focused to around 50 micrometers and controlled by a Brockton Electro-Optics Corp BEOC laser power controller. The laser was chopped with a NEOS Technology 15210 acousto-optic modulator (AOM) and paired with a Stanford Research Systems lock-in amplifier recording filtered light from a photodiode.

3.3.3 Microwave Generation and Amplification

Microwaves induce transitions between the Zeeman energy levels and are the fundamental variable modulated to retrieve ODMR data. The microwaves used for this experiment were produced using an Agilent Technologies E8257D microwave generator set at 10.4855 GHz at 0 dBm. A 20T4G18 traveling wave tube microwave amplifier increased the power of the microwaves up to about 40 dBM. The microwaves were then fed to a coupling loop placed next to the sample within

the cryostat.

3.3.4 Software Controller Interfaces and Data Recording

All experiments were conducted using a LabVIEW suite of programs designed to easily gather and record ODMR data. For our experiment, the LabVIEW suite controlled the microwave and laser modulating so that both could be referenced with a lock-in amplifier as necessary. The microwave generator and lock-in amplifier were interfaced using a GPIB addressing bus implemented as a separate class instantiation in the main LabVIEW program. The instrument classes were all designed to run in parallel to the main scanning software for better experimental isolation. The generic scanner object was built to handle an abstracted object implementing a "scannable" interface and another object implementing a "readable" interface. The scanner was built robustly enough to handle any combination of instrumentation that inherits from these two interfaces. It gives directives to the "scannable" object while also recording data from the "readable" object at the same time. A version of the program is linked-to in the introduction of this thesis and represents the ongoing work of myself, Ryan Peterson, Kyle Miller, Phil White, John Colton, and others.

In addition to the main LabVIEW suite of programs used, an additional VI was used to monitor the output of a magnetic field sensor provided by John Ellsworth. This was used to handle the magnetic field strength incident on our sample and make minor adjustments to the power-supply for the magnet according to measurements read off of the gaussmeter inserted into the field.

The overall program accepts as input a range of microwave frequencies and then records the absorption from the sample representing the ODMR. After this data was recorded, a graphing software known as *Origin* was used to produce plots from the raw data. The concluding chapter shows these results.

Chapter 4

Results

This chapter presents the ESR spectrum of SiC for both computational and experimental methods. The results of these two methods are then compared and contrasted and their strengths analyzed.

4.1 Computational Predictions

Using computational methods via spin Hamiltonian analysis with *EasySpin* we were able to recover the characteristic ESR spectrum shown in figure 4.1 using the spin paramaters in table 4.1. The figure shows resonant peaks at 10.35 GHz and 10.47 GHz for a field strength of 370.78 mT. Though there are only two major peaks, if we had defined our Hamiltonian further we may have been able to see smaller perturbation effects such as the fine and hyperfine structures.

Table 4.1 Summary of the spin Hamiltonian parameters for the defect center of interest in 4H-SiC. The spin-parity and g value is given for the isotropic defect center.

		Isotropic	
Center	S	g	φ (deg)
V_{Zn}^{-}	$3/2$	2.008	0

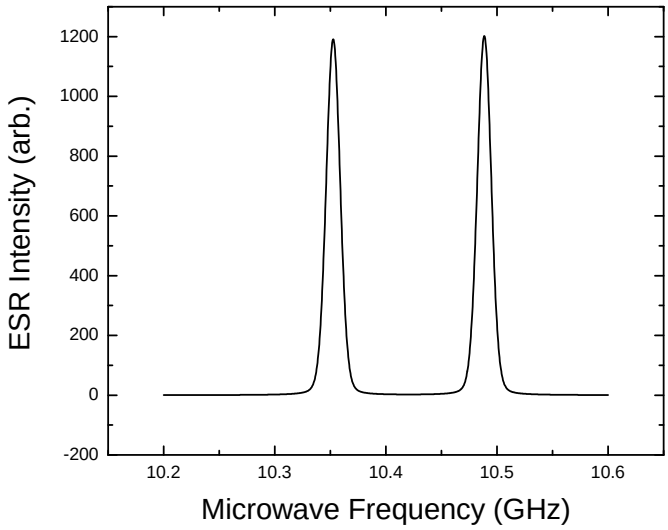

Figure 4.1 The uncorrected computational model for the ESR spectrum of 4H-SiC plotted for a magnetic field strength of B=370.78 mT. The plot shows the the relation between microwave frequency absorption for a static magnetic field strength.

4.2 Experimental Results

We successfully collected data showing the ODMR spectra for SiC. This data is shown in Figure 4.2. The same trend is seen in this data as is shown in the previous predictions. Namely, there are resonant peaks at 10.35 GHz and 10.47 GHz for a field strength of 370.78 mT. Also visible in this figure is a minor splitting of each peak visible at the very top of each spectral line. This is attributed to higher-order structures resulting from the perturbation of the material's energy levels.

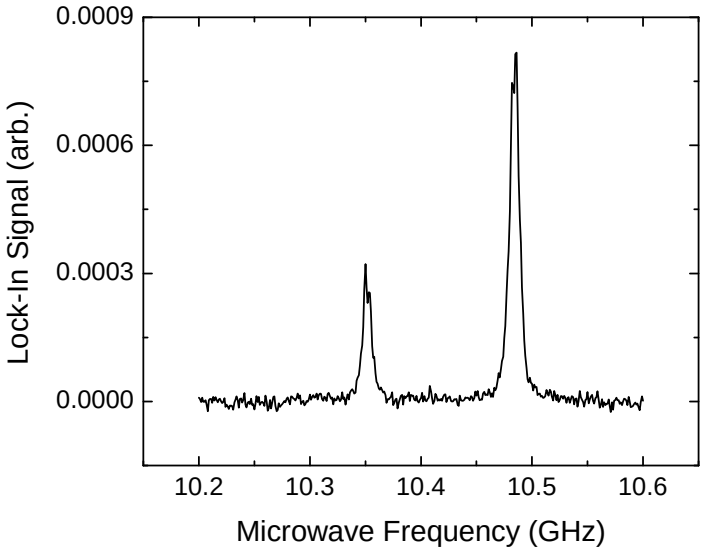

Figure 4.2 The experimental ODMR results for 4H-SiC for a magnetic field strength of B=370.78 mT. Like the computational predictions, this plot also shows the the relation between microwave frequency absorption for a static magnetic field strength.

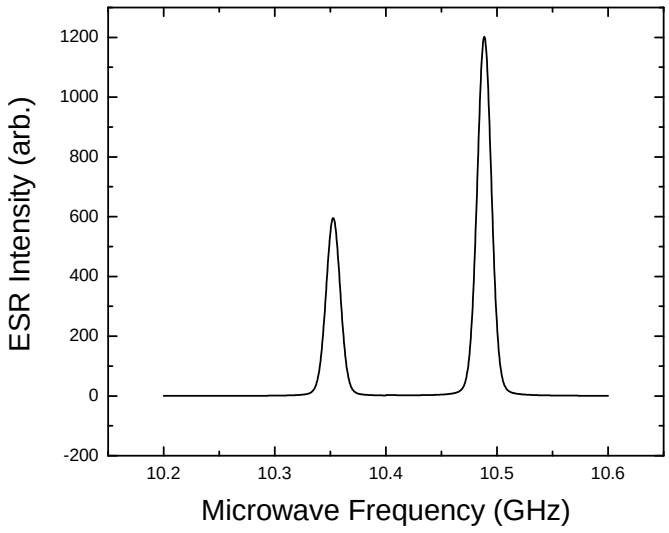

Figure 4.3 The manually-corrected computational model for the ESR spectrum of 4H-SiC plotted for a magnetic field strength of B=370.78 mT. In this plot the first minor peak has been corrected to reflect unaccounted Hamiltonian parameters

4.3 Data Analysis

The main expectation of the two different ESR methods is that both will produce spectral peaks at the same resonant microwave/magnetic field pairings. Moreover, it is also expected that the relative heights of each spectral peak are the same when compared between plots. The data presented in the previous sections corroborate at least the first of these two conditions. There is still is some differences between the two methods beyond these conditions. For example, the experimental ODMR shows a higher noise-floor than the computational method. It's easier to predict cleaner spectra when the only uncertainty is that of machine precision and not environmental effects.

It is expected (and actually acceptable) that there will be some variations in the results obtained between the experiment and the theoretical models. The most notable difference between the two methods is seen in the width of each spectral peak within the plots. Though it is similar, there is a quantitative difference between the two plots. Theoretically the probability of transitioning between microwave-levels in the samples should reach a delta-function limit centered at the resonant frequency for that given field strength. However, in practice this does not happen due to finite lifetimes and also due to inhomogeneities within the material itself. ESR peaks are instead shown to have finite widths in the magnetic-field domain. Though the experimental results are easily reproducible given the same parameters, different investigations may find different values of width depending on how the silicon carbide samples were produced. It is therefore not hard to explain why the computational predictions that were obtained for ESR do not always match the experimental results when there is such discrepancy among experimental procedures themselves. For our purposes a spectral line-width parameter was used to best match the experimental results that we obtained.

One of the major problems with modeling ESR spectra is that so many minor experimental conditions can fundamentally change the spin-system being studied and thus change what the resultant spectrum looks like when being modeled. As mentioned, computational models are only

effective to the extent that the Hamiltonian for the system is understood. For the case of silicon carbide, there is still many details about the material that are not well understood — or simply not known — about the system. For example, there is still a lot of speculation and ignorance regarding the exact effect of the nuclear-spin interaction, the effects of the ODMR PL-mechanism, and the effects of the inhomegenous distribution of defects in the sample. To account for this, Figure 4.3 shows the data from Figure 4.1 except with the spectral peaks treated separately in the Hamiltonian such that the relative peak-heights can be adjusted appropriately to match the experimental results.

4.4 Related Work

I have also included related work that I performed in addition to this thesis. The results are attached as appendices. The first appendix, Appendix A, is a publication of a study performed on 4H-SiC that I assisted with. The purpose of this study was to discover more fully what qualities lead to superior state coherence in spin-based quantum systems. For this paper we focused on two proton irradiated samples of SiC and used ODMR as the means to collect data from them. The second appendix, Appendix B, is an addendum to the first and includes data on a third electron irradiated sample of SiC. The works in both Appendix A and Appendix B present coherence times as a function of temperature for their respective samples of SiC. The final appendix, Appendix C includes the photoluminescence data on an ongoing investigation that I am performing on CdTe.

4.5 Conclusion

The primary conclusion of this thesis is that though there are some differences between the two methods, the results show that computational ESR predictions match experimental results to the same extent that the underlying Hamiltonian for that particular system is understood. In other words: the level of precision that computational modeling can present is restricted by how much

information is known about the Hamiltonian for that given system. Furthermore, there will always be some ambiguity between ODMR results and predictions due to practical considerations such as noise and ESR line-widths. Overall however, computational methods are good approximations of actual ESR results.

Appendix A

Electron Spin Coherence of Silicon Vacancies in Proton-Irradiated 4H-SiC

A large part of this thesis includes details about the semiconductor material known as silicon carbide. Optically detected magnetic resonance can be used with this material to discover important characteristics about its vacancy structure as it relates to electron spin coherence. In the attached paper, we report on the temperature-dependent T_2 spin coherence times and analyze what conditions lead to the varying coherence measurements across temperatures and irradiation fluence. We do this by comparing relative amplitude drops in a series of ODMR spectra taken from SiC for a given temperature. All experimental methods are laid forth and the final data is presented.

PHYSICAL REVIEW B **95**, 045206 (2017)

Electron spin coherence of silicon vacancies in proton-irradiated 4*H*-SiC

J. S. Embley,[1] J. S. Colton,[1,*] K. G. Miller,[1] M. A. Morris,[1] M. Meehan,[1] S. L. Crossen,[1]
B. D. Weaver,[2] E. R. Glaser,[2] and S. G. Carter[2]
[1]*Department of Physics and Astronomy, Brigham Young University, Provo, Utah 84602, USA*
[2]*Naval Research Laboratory, Washington, DC 20375, USA*

(Received 6 May 2016; revised manuscript received 20 October 2016; published 17 January 2017)

We report T_2 spin coherence times for electronic states localized in Si vacancies in 4*H*-SiC. Our spin coherence study included two SiC samples that were irradiated with 2 MeV protons at different fluences (10^{13} and 10^{14} cm^{-2}) in order to create samples with unique defect concentrations. Using optically detected magnetic resonance and spin echo, the coherence times for each sample were measured across a range of temperatures from 8 to 295 K. All echo experiments were done at a magnetic field strength of 0.371 T and a microwave frequency of 10.49 GHz. The longest coherence times were obtained at 8 K, being 270 ± 61 μs for the 10^{13} cm^{-2} proton-irradiated sample and 104 ± 17 μs for the 10^{14} cm^{-2} sample. The coherence times for both samples displayed unusual temperature dependencies; in particular, they decreased with temperature until 60 K, then increased until 160 K, then decreased again. This increase between 60 and 160 K is tentatively attributed to a motional Jahn-Teller effect. The consistently longer lifetimes for the 10^{13} cm^{-2} sample suggest that a significant source of the spin dephasing can be attributed to dipole-dipole interactions between Si vacancies or with other defects produced by the proton irradiation. The lack of a simple exponential decay for our 10^{14} cm^{-2} sample indicates an inhomogeneous distribution of defect spins.

DOI: 10.1103/PhysRevB.95.045206

I. INTRODUCTION

Electronic states localized in the defects of solids have shown great potential for important applications such as single photon emission [1,2], sensing [3], and quantum computing [4]. The nitrogen-vacancy defect center in diamond (N-V center) has been of particular interest in this regard. Applications such as quantum computing require quantum states that will remain coherent over a sufficiently long period of time [5]. Electrons spins in N-V centers can be controlled and manipulated, and through the use of dynamical decoupling pulse sequences have yielded coherence times of up to 3 ms at 300 K and 600 ms at 77 K [6]. However, the manufacture of appropriate diamond samples and integration into spintronic devices can be difficult and expensive, and thus there is strong interest in identifying other materials which may possess similar useful characteristics. Silicon carbide (SiC) is one such material which has shown significant promise, with similar properties to diamond but potentially easier fabrication [7].

There are many different polytypes of SiC [8]. Each polytype can have a variety of possible defects, and furthermore each defect type may possess unique spin properties [9–11]. Different defects in SiC can be formed and modified through high-energy particle bombardment [12] and annealing [13]. Using optically detected magnetic resonance (ODMR), defects in SiC can be optically initialized, addressed, and read out [14]. Individual defect spins can be isolated and coherently controlled [15,16]. The optical emission of silicon vacancies is longer in wavelength than that of the N-V center and has substantially less attenuation in optical fibers [7]. Silicon vacancy (V_{Si}) defects in SiC exhibit photoluminescence (PL) [17], can be individually controlled, and have spin coherence lifetimes on the order of 100 μs [16]. In 4*H*-SiC, the polytype studied in this paper, there are two inequivalent lattice sites where V_{Si} defects can exist, namely the hexagonal (h) and quasicubic (k) sites.

A variety of T_2 coherence time measurements have previously been made in 4*H*-SiC for electronic states in Si vacancies as well as for V_C-V_{Si} divacancy complexes. Native neutral divacancies' spin coherence times have been studied at a few different temperatures; one paper reported T_2 times of 360 μs at 20 K and 50 μs at 300 K [18], and another paper reported comparable times of 184 μs at 20 K (hk or kh divacancies) and 263 μs at 200 K (hh or kk divacancies) [19]. In a separate report at 20 K for one particular sample containing neutral divacancies formed through electron irradiation, measurements yielded T_2 times of up to 1.2 ms [15]. These types of coherence times are often measured through Hahn spin echo; however, through dynamical decoupling pulse sequences such as Carr-Purcell-Meiboom-Gill (CPMG), coherence times can typically be extended [19] as with the N-V center.

With regards to Si vacancies, an ensemble of V_{Si} defects formed through electron irradiation (2 MeV electrons at fluence of 10^{15} cm^{-2}) were measured to have a coherence time of 81 μs at room temperature [14]. A separate study on a similar sample, with Si vacancies formed through electron irradiation, showed T_2 times at room temperature of 160 μs [16]. Finally, a maximum coherence time on the order of hundreds of milliseconds was achieved at 17 K for Si vacancies using dynamic decoupling pulses [20].

Although some of these works have measured the spin coherence times at two temperatures, none has addressed the temperature dependence of T_2 in a systematic fashion. By contrast, the T_1 and T_2^* lifetimes of vacancy defects in SiC have been measured over a range of temperatures by at least two groups. The T_1 of Si vacancies decreased monotonically with increasing temperature [20], whereas the T_2^* of divacancies had a complicated, nonmonotonic dependence [21].

In this paper we report T_2 lifetimes for electrons localized at Si vacancies in 4*H*-SiC, a polytype which has demonstrated

*Corresponding author: john_colton@byu.edu

 ©2017 American Physical Society

significant potential [19]. Measurements were made on two distinct samples, in which the V_{Si} defects in the two samples were created with different fluences of proton irradiation: 10^{13} and 10^{14} cm^{-2}. Temperatures from 8 to 295 K were studied. The highest T_2 time for each sample was found at the lowest temperature (8 K): the 10^{13} cm^{-2} sample with a lifetime of 270 ± 61 μs and the 10^{14} cm^{-2} sample with a lifetime of 104 ± 17 μs. The lifetimes for each sample decrease with temperature until about 60 K, then unexpectedly increase from 60 until 160 K, after which they decrease again. This unusual trend with temperature is very similar to what was seen in SiC divacancy measurements by Falk *et al.*, their overall T_2^* lifetimes being four orders of magnitude shorter than our T_2 lifetimes but in many respects following a similar temperature trend [21]. This trend is tentatively attributed to dynamic averaging from a motional Jahn-Teller effect as has been seen in the C vacancy [22].

II. EXPERIMENTAL METHODS

Each sample consists of high purity semi-insulating SiC (from Cree, Inc.) with the *c* axis oriented 8° from the normal to the sample. Si vacancies were generated by irradiating four pieces of the same SiC wafer with 2 MeV protons at fluences of 10^{11}, 10^{12}, 10^{13}, and 10^{14} cm^{-2}. (The vacancy concentration pre-irradiation was negligible.) The 10^{11} cm^{-2} sample was used for spatially-resolved PL to estimate defect concentration, the 10^{12} cm^{-2} sample for depth-dependent PL, and all of the spin-related measurements were made on the 10^{13} and 10^{14} cm^{-2} samples alone. The PL spectra of the 10^{13} and 10^{14} cm^{-2} samples are displayed in Fig. 1; the "V2" line at 916 nm marks the V_{Si} PL emission from the *h* defect site that we used in the spin experiments presented below. We note that the other sharp PL line of comparable intensity observed in this spectral range at 930 nm is not identified at this time.

Defect formation through proton irradiation is of particular interest because the protons have a well-defined stopping distance. It is therefore a step towards controlled patterned placement of these defect centers, as has been done with ion implantation. For example, Falk *et al.* used 10 keV energy ^{12}C ions at a dose of 10^{13} cm^{-2} to implant divacancy spin ensembles in SiC in a patterned array [18]. From our SRIM (stopping and range of ions in matter) simulations, the stopping range of the 2 MeV protons is predicted to be 44 μm from the surface. Depth-dependent PL of the 10^{12} cm^{-2} sample shows bright V2 emission centered at a depth of 34 μm, which we interpret as the actual stopping range of the protons; see Fig. 2. This was measured via confocal microscopy on a cleaved edge of the sample, scanning normal to the surface using a 0.7 numerical aperture objective, 780 nm excitation, and at a temperature of 25 K. As can be seen from the figure, the V2 PL—and hence the vacancy defects themselves—extends from the surface to the stopping layer. The vacancies exist in two regimes: a diffuse region ranging from the surface to the stopping layer, and a more concentrated region at the stopping layer itself. The integrated area of the peak vs that for the diffuse region is larger by about a factor of 3.

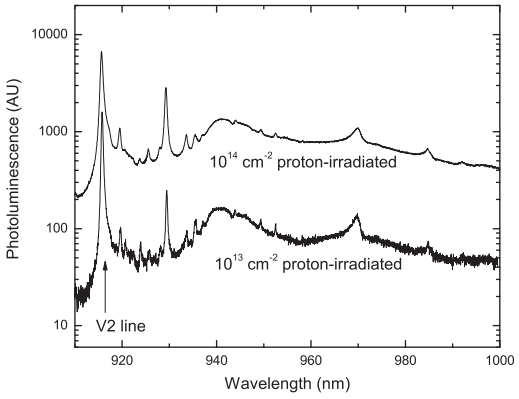

FIG. 1. Photoluminescence of the two main SiC samples with 870 nm excitation. Note the order-of-magnitude increased strength of the spectral peaks for the 10^{14} cm^{-2} sample as compared to the 10^{13} cm^{-2} sample, due to the increased number of vacancy defects. The spectra were both taken at low temperature (5 and 6 K for the 10^{14} and 10^{13} cm^{-2} samples, respectively).

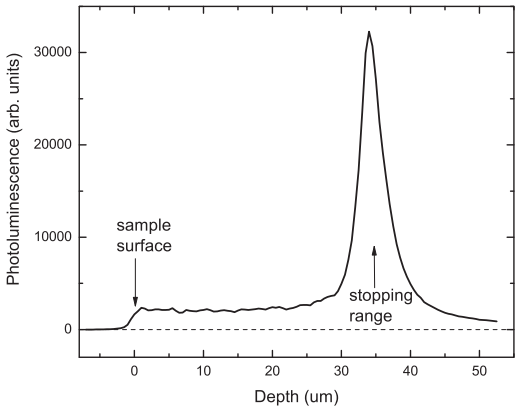

FIG. 2. Depth-dependent photoluminescence of the 10^{12} cm^{-2} sample at the V2 wavelength. The large peak at 34 μm indicates the stopping position of the protons. The spatial resolution was 1 μm.

Photoluminescence from individual vacancies was resolved in the 10^{11} cm^{-2} sample in the diffuse region, also via confocal microscopy, leading to an estimate of 0.3 defects/μm^3 (3×10^{11} cm^{-3}) for that sample. This is only an order of magnitude estimate since we did not have sufficient emission rate to verify that the PL sources were single emitters by, e.g., correlated photon antibunching measurements. Assuming the number of defects scales linearly with radiation dose, we estimate the V_{Si} densities of the other three samples to be 3, 30, and 300 μm^{-3}, i.e., 3×10^{12}, 3×10^{13}, and 3×10^{14} cm^{-3}, for their diffuse regions. The densities in the more concentrated regions are estimated to be about 10 times higher than those based on the depth-dependent PL.

For all of the spin experiments, the samples were placed in a nonmagnetic CryoIndustries cryostat mounted inside a large conventional iron-core electromagnet, with the field perpendicular to the sample face (i.e., 8° from the *c* axis).

The current for the electromagnet was provided by a Magna-Power Electronics power supply targeting a field strength of 0.371 T and operating in a mode where the output voltage follows an input analog reference voltage. The reference voltage was determined by the built-in PI controller of a Lake Shore Cryotronics gaussmeter whose probe was mounted in the magnet near the sample. Operating the magnet in this configuration provided a field stability of 0.03 mT.

We used an optically pumped Spectra-Physics cw Ti:sapphire laser tuned to 870 nm to align the spins and induce PL from the sample. The laser was stabilized by a BEOC laser power controller (long-term stability of 0.03%) and then focused onto a NEOS Technologies acousto-optic modulator (AOM), which allowed for optical pulses as short as 20 ns. The laser beam was expanded, re-collimated, then focused onto the sample with a cw-equivalent power of about 350 mW (i.e., the power if the laser had a duty cycle of 100%) and a spot size approximately 100 μm in diameter. The light impacted the sample edge-on, with the vertical polarization direction being along the plane of the surface. Due to the spot size, the depth of the defects as shown in Fig. 2, and the edge-on nature of the alignment, the laser therefore probes defects from all depths and a variable range of defect densities. We employed a 900 nm long pass dichroic mirror/beam splitter which reflects the laser beam but allows the emitted PL (at about 915 nm) to pass through. Additionally, three 900 nm long pass filters were placed in front of the detector (a Newport 818-SL photodiode) to reduce the amount of scattered laser light mixed in with the PL. Between the beam splitter and filters, scattered laser light at the detector was reduced by a nominal factor of 3×10^{10}.

Microwaves at 10.49 GHz, produced by an Agilent Technologies synthesizer at 0 dBm and increased by an Amplifier Research traveling wave tube amplifier to 40 dBm, were used to manipulate the electronic spins. The microwaves were transmitted to the sample via a small coupling loop surrounding the sample, formed by shorting the inner and outer conductors of a coaxial cable. The frequency near 10.49 GHz was selected and a stub tuner was employed to maximize microwave transmission through the loop. The coupling loop was oriented so that the ac magnetic field from the microwaves was orthogonal to the dc field of the electromagnet. See Fig. 3 for a schematic of the optics and the relative orientations of the sample, static magnetic field, microwave field, and laser beam. The microwaves were modulated on and off via a PIN diode switch controlled by an Agilent pulse pattern generator, which also controlled the AOM. When microwave pulse sequences were

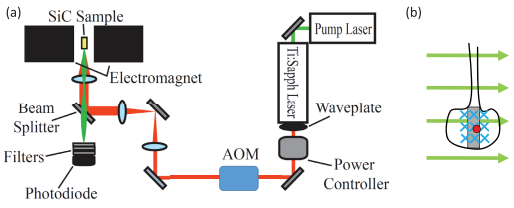

FIG. 3. (a) Schematic of the optical experiment. (b) View of microwave coupling loop (black) and sample (gray) in cryostat, with static magnetic field (green arrows), microwave field (blue arrow tails), and laser beam (red dot, vertically polarized) indicated.

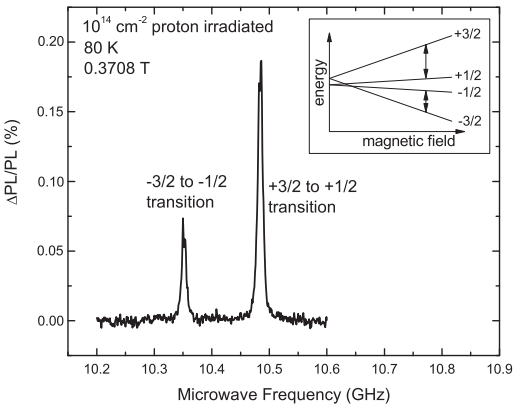

FIG. 4. Representative optically detected magnetic resonance of the 10^{14} cm^{-2} proton-irradiated sample, at 80 K and 0.3708 T. Two peaks are observed. The signal strength is plotted as a percentage of the total photoluminescence reaching the detector. Inset: Energy levels of the spin 3/2 system, with the two observed transitions indicated. The $+3/2 \leftrightarrow +1/2$ transition was used for all echo scans.

employed for Rabi and spin echo scans, the sequences were gated on and off at 1 kHz with a Tektronix function generator.

The ground state of the V_{Si} defect in 4H-SiC forms a spin 3/2 state [14,23,24]. The inset to Fig. 4 depicts the four energy levels schematically. Transitions between the $m_s = +3/2$ and $+1/2$, and between the $-1/2$ and $-3/2$ states can be observed through ODMR as two peaks separated by 135 MHz; see Fig. 4. We chose to focus on the $+3/2 \leftrightarrow +1/2$ transition, i.e., the higher frequency peak. The ODMR signal at the peak varied from about 0.4% of the PL at low temperatures to 0.1% of the PL at room temperature. The mechanism by which the ODMR occurs involves a spin-dependent nonradiative transition through a metastable state. As a result of this spin-dependent transition, optical pumping with linearly polarized light causes the $\pm 1/2$ states to become preferentially populated over the $\pm 3/2$ states [16] (or possibly the $\pm 3/2$ states may be preferentially populated over the $\pm 1/2$ states [25], there is some dispute in the literature). This spin dependent nonradiative process also results in less PL when the system is in this optically pumped set of states [7]. When microwaves induce transitions between the $+1/2$ and $+3/2$ states, the populations are equalized causing PL to increase. Thus, the relative amount of PL detected by the photodiode is reflective of the current state of the spins. To detect such changes we connected the photodiode detector to a Stanford Instruments lock-in amplifier in current mode referenced to the overall microwave pulse sequence on/off gating frequency; the data in Fig. 4 employed a 50% duty cycle.

III. MICROWAVE PULSE SEQUENCES

The two observed transitions can be described by the equations $f_{\text{lower}} = -67.3\ \text{MHz} + 28.10\frac{\text{GHz}}{\text{T}} \times B$ and $f_{\text{upper}} = +67.3\ \text{MHz} + 28.10\frac{\text{GHz}}{\text{T}} \times B$, where f is frequency

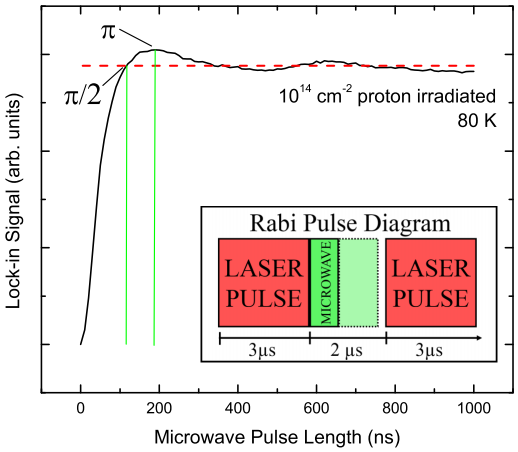

FIG. 5. Representative Rabi oscillation data, for the 10^{14} cm^{-2} sample at 80 K. The vertical lines (green) represent the π and $\pi/2$ pulse times deduced from the experiment for those conditions. The horizontal dashed line (red) indicates the zero polarization value. Inset: The laser and microwave pulse sequences for the Rabi experiments.

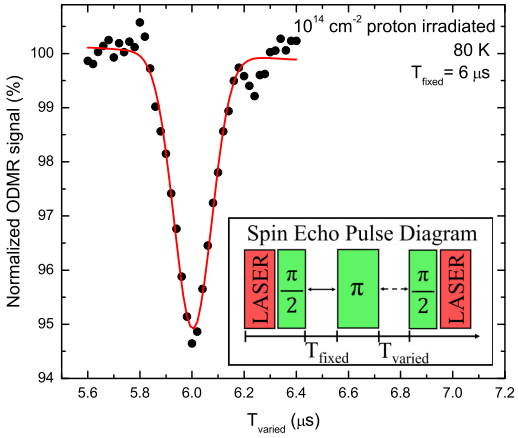

FIG. 6. Representative spin echo data, for the 10^{14} cm^{-2} sample at 80 K and with a T_{fixed} value of 6 μs. The data is normalized so that the y axis is the ODMR signal divided by the ODMR baseline. The red line represents a Gaussian fit of the data with a linear baseline. The echo strength is defined to be how far the echo changes from 100% towards zero. Inset: The laser and microwave pulse sequences for the spin echo experiments.

and B is the magnetic field strength. The slope of the frequency vs B relates to the electron g factor; the measured slope gives rise to a g factor of $g = 2.007$, which is very close to the free electron value of 2.002. These parameters are in good agreement with other measured V2 parameters from the literature [26]. We detect the resonance condition by fixing the static magnetic field and scanning the applied microwaves across a range of frequencies while observing the PL signal.

The spin echo technique requires $\pi/2$ and π microwave pulses to manipulate the spin states. The appropriate lengths of these pulses were determined by observing Rabi oscillations. The Rabi oscillation scans were done with a 3 μs laser pulse followed by a variable microwave pulse (between 0 and 2 μs); the two pulses were repeated with a frequency of 174 kHz, i.e., a little slower than $1/(3\,\mu\text{s} + 2\,\mu\text{s})$. The laser pulses serve the dual purpose of stimulating PL, which allows the current state of the spins to be read out, and re-initializing the spins for the next period. The variable length microwave pulse causes the spins to flip between the two spin states, resulting in an oscillating PL response. We defined the π pulse length as the time where the PL reaches its first maximum, and the $\pi/2$ pulse as the time when the PL reaches its first zero polarization value; see Fig. 5 for a representative case at 80 K where the $\pi/2$ and π pulse lengths were 117 and 189 ns, respectively. The $\pi/2$ and π pulse lengths were established for each temperature independently in a similar fashion. The strong damping indicates a large amount of inhomogeneous dephasing, with T_2^* times on the order of a few hundred nanoseconds.

As shown in the insert to Fig. 6, the pulse sequence for the spin echo experiments was as follows: a 3 μs pulse from the laser, a $\pi/2$ microwave pulse to rotate the spins 90° into a superposition of the two states, a time delay (T_{fixed}) during which the spins precess and dephase due to inhomogeneity, a π microwave pulse to rotate the states another 180°, a second time delay (T_{varied}) to allow the spins to rephase, and finally a second $\pi/2$ microwave pulse to rotate the spins back to their initial state for read-out. For each echo scan, we set a value for T_{fixed} then took data as a function of T_{varied} values. The frequency for the overall pulse sequence was chosen based on the total time required for the laser and microwave pulses and the T_{fixed} and T_{varied} delays, ranging from 165 down to 6 kHz. A representative spin echo scan is plotted in Fig. 6; the minimum corresponds to the echo and is obtained when $T_{\text{varied}} = T_{\text{fixed}}$. The spin echo is a negative effect because the ODMR signal *increases* when coherence is *lost*; conversely, if phase coherence is retained the electrons will end up in their initial state at the end of the pulse sequence which reduces the signal. For perfect pulse rotations and rephasing, the echo should bring the ODMR signal to zero, but T_2^* limits the rotation fidelity here, as evidenced by the heavily damped Rabi oscillations.

The echoes were well fit to negative Gaussian peaks with linear baselines, and the strength of each echo was characterized as how far the signal dipped from the baseline (plotted as 100%) toward zero. Note that a 5% echo strength, as is for example the case for Fig. 6, represents a 5% change in the ODMR signal, meaning 5% of the "ΔPL/PL" signals discussed above and plotted in Fig. 4 (which were 0.1%–0.4%).

IV. RESULTS AND DISCUSSION

For a given temperature, the echo signal decreases in strength as T_{fixed} is increased; this indicates that spin coherence is being lost as a function of time. Representative decays are displayed for both samples in Fig. 7. In the simplest case, the

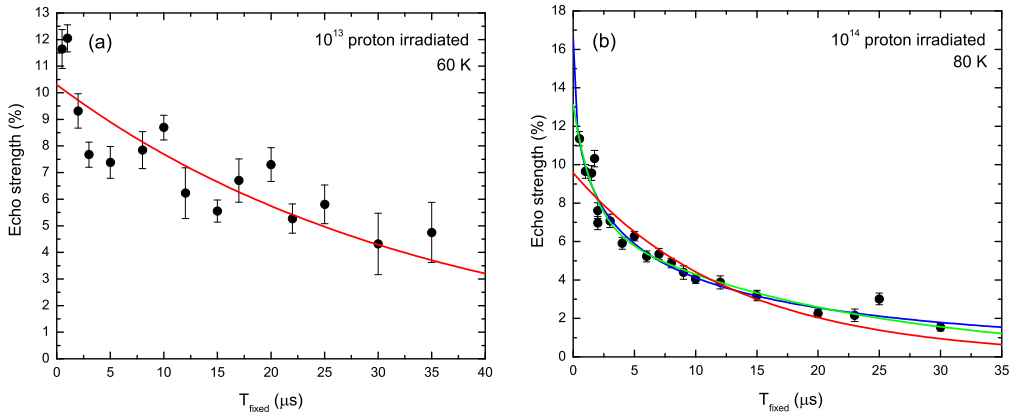

FIG. 7. Representative echo decays for both samples. (a) The 10^{13} cm^{-2} sample at 60 K. The red line is an exponential decay fit as per Eq. (1). (Noise prohibited data collection in for T_{fixed} values longer than 35 μs.) (b) The 10^{14} cm^{-2} sample at 80 K. The red line is an exponential decay fit [Eq. (1)]; the green line is a biexponential decay fit [Eq. (2)]; the blue line is a stretched exponential fit [Eq. (3)], which overlaps the biexponential fit for most of the decay.

echo strength (y) will decay as

$$y = Ae^{-\frac{2T_{\text{fixed}}}{\tau}}, \tag{1}$$

where the fitting parameter τ represents the T_2 spin lifetime. The factor of 2 arises because the total time scale is set by the sum of T_{fixed} and T_{varied}.

Our data for the 10^{14} cm^{-2} sample in many cases cannot be well fit by the simple exponential decay of Eq. (1). We found that, instead, the data can much better be fit either as the sum of two exponential decays,

$$y = A_1 e^{-\frac{2T_{\text{fixed}}}{\tau_{\text{short}}}} + A_2 e^{-\frac{2T_{\text{fixed}}}{\tau_{\text{long}}}}, \tag{2}$$

where the parameters τ_{short} and τ_{long} represent decay times of two different populations of defect spins; or as a stretched exponential,

$$y = Ae^{-(\frac{2T_{\text{fixed}}}{\tau})^{\beta}}, \tag{3}$$

where τ represents a characteristic spin coherence time and β characterizes the width of a continuous distribution of times (the distribution going to a delta function in the limit that β approaches 1). There is no *a priori* reason to favor one functional form over the other and therefore we have fit our data for the 10^{14} cm^{-2} sample to both Eqs. (2) and (3). Figure 7(b) demonstrates the fits for the biexponential and stretched exponential decays (green and blue curves, respectively), along with a single exponential decay (red). Much better fits are obtained using Eqs. (2) and (3). Equation (2) would imply a bimodal distribution of lifetimes, which is plausible given the distribution of V_{Si} defects as shown in Fig. 2, i.e., some vacancies being present in a highly concentrated region and some being present in a more diffuse layer. However, the values of A_2 (long time component) obtained from the fits are always larger than the values of A_1 (short time component). This is reversed from what one would expect if the two components of the biexponential fit were to directly correspond to the two types of defect distributions seen in Fig. 2, because one would expect the concentrated region with higher integrated PL to have shorter lifetimes than the diffuse region with lower integrated PL. Therefore in the Eq. (2) fit results, the two terms of the biexponential fit are unlikely to directly correspond to the two types of defect distributions.

Equation (3), in contrast, would imply a continuous distribution of lifetimes, where the parameter β is a measure of the distribution width; when $\beta > 1$ this is a compressed (rather than stretched) exponential function and has been used by others to phenomenologically fit spin echo decay in SiC (with $\beta = 2$) [15]. From our fits of these samples we find $\beta < 1$, i.e., the more normal stretched case; the typical values of β from our fits would correspond to lifetime distributions having FWHM values ranging from 2.5–14 τ and mean T_2 coherence times of 1.3–3.3 τ. Either way, the lack of a single exponential decay time likely indicates inhomogeneity, which is consistent with both the rapid dephasing of the Rabi oscillations (as shown in Fig. 5) and the distributions of defect densities from the vacancy depth profile.

For the 10^{13} cm^{-2} sample results, due to the increased amount of noise (a result of less PL and longer decay times, which require smaller duty cycles) we could not definitively conclude that a simple single exponential decay was insufficient to fit the data; thus we present in Table I and Fig. 8(a) only a single decay time in the results for this sample. For completeness, in Table II we include the fitting parameters obtained from both Eqs. (2) and (3), although for simplicity Fig. 8(b) just includes the Eq. (2) value of τ_{long} for the 10^{14} cm^{-2} sample. As can be readily seen, the spin coherence times for the 10^{13} cm^{-2} sample for most temperatures are a factor of 1.5–2.5 larger than the coherence times of the 10^{14} cm^{-2} sample (comparing vs the τ_{long} values).

The longest coherence times are found at the lowest temperatures and in general decrease as the temperature is increased, but surprisingly the lifetimes increase from about 60 until 160 K, before decreasing again. When the overall trend is viewed, the coherence times in both samples appear

TABLE I. Fitted spin lifetimes for the 10^{13} cm^{-2} proton irradiated sample.

Temperature (K)	Single exponential fit τ (μs)
8	270 ± 61
20	110 ± 55
30	105 ± 28
40	45 ± 10
60	69 ± 14
90	41 ± 8
120	55 ± 11
160	164 ± 30
190	32 ± 9

to be enhanced in the region from 60 to 160 K. This behavior is remarkable, as the dominant spin dephasing mechanisms usually result in a continuous decrease of spin lifetime with temperature. For example, in both experimental and theoretical studies of the T_1 spin lifetime of the V_{Si} defect in SiC, T_1 vs temperature changes monotonically from 5 to 300 K as a result of phonon-assisted spin relaxation mechanisms [20].

As a possible explanation for the increase in spin coherence time in the 60–160 K region, we suggest the dynamic Jahn-Teller effect. A similar nonmonotonic temperature behavior has been seen in the positively charged carbon vacancy V_C

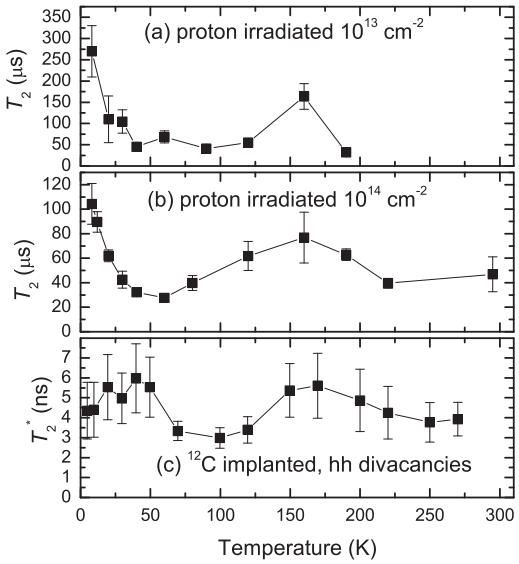

FIG. 8. Temperature dependence of spin lifetimes in SiC. The black connecting lines serve as guides to the eye. (a) T_2 coherence times of 10^{13} cm^{-2} 4H-SiC sample. (Noise prohibited data collection for temperatures higher than 190 K.) (b) T_2 coherence times of 10^{14} cm^{-2} 4H-SiC sample (biexponential τ_{long} values). (c) T_2^* times of SiC *hh* divacancies. Figure 7(c) adapted with permission from Ref. [21]. Copyrighted by the American Physical Society.

TABLE II. Fitted spin lifetimes for the 10^{14} cm^{-2} proton irradiated sample.

Temperature	Biexponential fit		Stretched exponential fit	
(K)	τ_{short} (μs)	τ_{long} (μs)	β	τ (μs)
8	8 ± 5	104 ± 17	0.6 ± 0.1	79 ± 6
12	9 ± 5	90 ± 8	0.7 ± 0.1	70 ± 3
20	1.1 ± 0.4	62 ± 5	0.4 ± 0.1	34 ± 11
30	6 ± 4	43 ± 7	0.7 ± 0.1	28 ± 3
40	1.3 ± 1.0	32 ± 2	0.6 ± 0.1	21 ± 3
60	1.8 ± 0.6	28 ± 3	0.4 ± 0.1	8 ± 3
80	3 ± 1	40 ± 6	0.4 ± 0.1	9 ± 5
120	7 ± 3	62 ± 12	0.6 ± 0.1	34 ± 3
160	12 ± 9	77 ± 21	0.7 ± 0.1	51 ± 4
190	2.3 ± 0.6	63 ± 5	0.5 ± 0.1	32 ± 6
220	1.7 ± 1.4	40 ± 4	0.7 ± 0.1	30 ± 3
295	5 ± 3	47 ± 14	0.5 ± 0.1	22 ± 5

of 4H-SiC [22]. In that work, the authors found that the low temperature vacancy structure was characterized by the pairing of orbitals of the four neighboring Si atoms due to Jahn-Teller distortion (Si1-Si2 and Si3-Si4). Dynamic reorientation at higher temperatures was seen through the effects of EPR and pulsed EPR on the V_C hyperfine lines. The authors measured T_2 through the spin echo decay as well as through the width of resonance lines. They found two regimes: below 40 K they observed lifetime broadening where T_2 decreased with temperature. Above 40 K they found motional narrowing where T_2 increased with temperature. The motional narrowing was attributed to a thermally activated reorientation of the vacancy, with a 14 meV activation energy. In other words, rapid thermally activated reorientations (bond switching) change the character of the vacancy, and cause the spin lifetime to increase rather than decrease with temperature.

A similar temperature dependence to our T_2 data was seen for T_2^* by Falk *et al.* [21] in V_C-V_{Si} divacancies in 6H-SiC. We have plotted their data for *hh* divacancies in Fig. 8(c). Aside from the initial rise in lifetime with temperature, their data displays a very similar temperature dependence to our own. They also observed a similar effect for *kk* divacancies which for simplicity we have not plotted. Their T_2^* times are four orders of magnitude smaller than our T_2 times, which makes the similarity in temperature dependence all the more striking. They also attribute some of the nonmonotonic behavior to the motional narrowing/dynamic Jahn-Teller effect. The similarities between SiC vacancy-related spin lifetimes seen in the V_{Si} (this work), the V_C [22], and the V_{Si}-V_C divacancy [21], despite differences in samples and defect centers, seem to indicate that the motional Jahn-Teller effect may play a fundamental role in affecting spin dephasing in such materials.

Lastly, we note that the times for the 10^{13} cm^{-2} sample were consistently longer than for the 10^{14} cm^{-2} sample. This suggests that a significant source of the spin dephasing can be attributed to dipole-dipole interactions with proton-irradiation induced defects; the interactions could be between two nearby V_{Si} centers or between a V_{Si} center and other defects. Other studies have found dipole-dipole interactions to be the dominant factor in dephasing in V_{Si}

centers [16,26]. For example, Widmann *et al.* [16] estimated that concentrations of $10^{16}\,\mathrm{cm}^{-3}$ spins should give rise to $\sim 100\,\mu\mathrm{s}$ spin decoherence times, with time being inversely proportional with spin concentration. This is fairly consistent with our results, although an exact inverse scaling, ignoring other mechanisms, would predict times of $\sim 3000\,\mu\mathrm{s}$ in the concentrated region of the $10^{13}\,\mathrm{cm}^{-2}$ irradiated sample (V_{Si} concentration of $\sim 3 \times 10^{14}\,\mathrm{cm}^{-2}$ in that region) and $\sim 300\,\mu\mathrm{s}$ in the concentrated region of the $10^{14}\,\mathrm{cm}^{-2}$ irradiated sample (V_{Si} concentration of $\sim 3 \times 10^{15}\,\mathrm{cm}^{-3}$ in that region). Of course other radiation-induced defects will also be present, and our measured lifetimes being lower than those predictions from the scaling may indicate that important dipole-dipole interactions may also be going on between the V_{Si} centers and other radiation-induced defects (possibly carbon vacancies or divacancies), as well as between the V_{Si} centers themselves.

V. CONCLUSION

We have measured T_2 spin coherence times for electronic states of the V_{Si} defect center in proton-irradiated 4H-SiC. The coherence times were as long as 270 μs for the $10^{13}\,\mathrm{cm}^{-2}$ proton-irradiated sample at 8 K. In addition, the times for the $10^{13}\,\mathrm{cm}^{-2}$ sample were consistently longer than for the $10^{14}\,\mathrm{cm}^{-2}$ sample, which indicates dipole-dipole interactions with radiation-induced defects are a source of dephasing. The coherence times followed a nonmonotonic dependence on temperature, with the unexpected rise in lifetime with temperature in the 60–160 K range possibly explained by motional narrowing arising from a dynamic Jahn-Teller effect similar to what has been observed in the V_{C} [22], and the V_{Si}-V_{C} divacancy [21]. Lastly, the lack of a simple exponential decay for the $10^{14}\,\mathrm{cm}^{-2}$ proton-irradiated sample points to an inhomogeneous population of defect spins, possibly a bimodal distribution or one with a more complex distribution of lifetimes. This may be due to our sampling of regions of varying defect density inside the optical focus.

ACKNOWLEDGMENTS

J.S.E., K.G.M., and M.A.M. were partially or fully supported through the NSF REU program, Grant No. PHY-1461219. M.A.M. was a visiting student from Brandeis University. S.G.C. and E.R.G. acknowledge support from the U.S. Office of Naval Research and the OSD ARAP Quantum Sciences and Engineering Program. The authors also thank Michel Bockstedte for a helpful theoretical discussion.

[1] S. Castelletto, B. C. Johnson, V. Ivády, N. Stavrias, T. Umeda, A. Gali, and T. Ohshima, Nat. Mater. **13**, 151 (2014).
[2] A. Lohrmann, N. Iwamoto, Z. Bodrog, S. Castelletto, T. Ohshima, T. J. Karle, A. Gali, S. Prawer, J. C. McCallum, and B. C. Johnson, Nat. Commun. **6**, 7783 (2015).
[3] H. Kraus, V. A. Soltamov, F. Fuchs, D. Simin, A. Sperlich, P. G. Baranov, G. V. Astakhov, and V. Dyakonov, Sci. Rep. **4**, 5303 (2014).
[4] R. J. Epstein, F. M. Mendoza, Y. K. Kato, and D. D. Awschalom, Nat. Phys. **1**, 94 (2005).
[5] C. H. Bennett and D. P. DiVincenzo, Nature (London) **404**, 247 (2000).
[6] N. Bar-Gill, L. M. Pham, A. Jarmola, D. Budker, and R. L. Walsworth, Nat. Commun. **4**, 1743 (2013).
[7] P. G. Baranov, A. P. Bundakova, A. A. Soltamova, S. B. Orlinskii, I. V. Borovykh, R. Zondervan, R. Verberk, and J. Schmidt, Phys. Rev. B **83**, 125203 (2011).
[8] F. Bechstedt, P. Käckell, A. Zywietz, K. Karch, B. Adolph, K. Tenelsen, and J. Furthmüller, Phys. Status Solidi (b) **202**, 35 (1997).
[9] D. Riedel, F. Fuchs, H. Kraus, S. Väth, A. Sperlich, V. Dyakonov, A. A. Soltamova, P. G. Baranov, V. A. Ilyin, and G. V. Astakhov, Phys. Rev. Lett. **109**, 226402 (2012).
[10] V. A. Soltamov, A. A. Soltamova, P. G. Baranov, and I. I. Proskuryakov, Phys. Rev. Lett. **108**, 226402 (2012).
[11] N. T. Son, P. Carlsson, J. ul Hassan, E. Janzén, T. Umeda, J. Isoya, A. Gali, M. Bockstedte, N. Morishita, T. Ohshima, and H. Itoh, Phys. Rev. Lett. **96**, 055501 (2006).
[12] H. Itoh, N. Hayakawa, I. Nashiyama, and E. Sakuma, J. Appl. Phys. **66**, 4529 (1989).
[13] W. E. Carlos, N. Y. Garces, E. R. Glaser, and M. A. Fanton, Phys. Rev. B **74**, 235201 (2006).
[14] S. G. Carter, Ö. O. Soykal, P. Dev, S. E. Economou, and E. R. Glaser, Phys. Rev. B **92**, 161202 (2015).
[15] D. J. Christle, A. L. Falk, P. Andrich, P. V. Klimov, J. U. Hassan, N. T. Son, E. Janzén, T. Ohshima, and D. D. Awschalom, Nat. Mater. **14**, 160 (2015).
[16] M. Widmann, S.-Y. Lee, T. Rendler, N. T. Son, H. Fedder, S. Paik, L.-P. Yang, N. Zhao, S. Yang, I. Booker, A. Denisenko, M. Jamali, S. A. Momenzadeh, I. Gerhardt, T. Ohshima, A. Gali, E. Janzén, and J. Wrachtrup, Nat. Mater. **14**, 164 (2015).
[17] E. Sörman, N. T. Son, W. M. Chen, O. Kordina, C. Hallin, and E. Janzén, Phys. Rev. B **61**, 2613 (2000).
[18] A. L. Falk, B. B. Buckley, G. Calusine, W. F. Koehl, V. V. Dobrovitski, A. Politi, C. A. Zorman, P. X. L. Feng, and D. D. Awschalom, Nat. Commun. **4**, 1819 (2013).
[19] W. F. Koehl, B. B. Buckley, F. J. Heremans, G. Calusine, and D. D. Awschalom, Nature (London) **479**, 84 (2011).
[20] D. Simin, H. Kraus, A. Sperlich, T. Ohshima, G. V. Astakhov, and V. Dyakonov, arXiv:1602.05775.
[21] A. L. Falk, P. V. Klimov, V. Ivády, K. Szász, D. J. Christle, W. F. Koehl, Á. Gali, and D. D. Awschalom, Phys. Rev. Lett. **114**, 247603 (2015).
[22] T. Umeda, J. Isoya, N. Morishita, T. Ohshima, T. Kamiya, A. Gali, P. Deák, N. T. Son, and E. Janzén, Phys. Rev. B **70**, 235212 (2004).
[23] H. Kraus, V. A. Soltamov, D. Riedel, S. Vath, F. Fuchs, A. Sperlich, P. G. Baranov, V. Dyakonov, and G. V. Astakhov, Nat. Phys. **10**, 157 (2014).

[24] N. Mizuochi, S. Yamasaki, H. Takizawa, N. Morishita, T. Ohshima, H. Itoh, and J. Isoya, Phys. Rev. B **66**, 235202 (2002).
[25] Ö. O. Soykal, P. Dev, and S. E. Economou, Phys. Rev. B **93**, 081207 (2016).
[26] V. A. Soltamov, B. V. Yavkin, D. O. Tolmachev, R. A. Babunts, A. G. Badalyan, V. Y. Davydov, E. N. Mokhov, I. I. Proskuryakov, S. B. Orlinskii, and P. G. Baranov, Phys. Rev. Lett. **115**, 247602 (2015).

Appendix B

Electron Spin Studies of Electron Irradiated SiC

Following the same experimental details and methods found in Appendix A, I have collected the temperature-dependent T_2 times for an electron-irradiated sample of SiC irradiated at a fluence of 10^{17} cm^{-2}. As with the proton irradiated samples, the electron irradiated sample exhibited a decrease in echo signal as T_{fixed} increased. This relation could be then fit using common regression techniques so as to characterize the overall spin coherence paramater *tau*. The final data is presented in three ways. First, Figure B.1 displays the parameter τ in the echo strength-decay formula $y = Ae^{-\frac{2T_{\text{fixed}}}{\tau}}$. Second, Figure B.2 displays the fitted τ_{long} in the regression $y = A_1 e^{-\frac{2T_{\text{fixed}}}{\tau_{\text{short}}}} + A_2 e^{-\frac{2T_{\text{fixed}}}{\tau_{\text{long}}}}$. Finally, Figure B.3 shows τ from the fitted formula $y = Ae^{-(\frac{2T_{\text{fixed}}}{\tau})^{\beta}}$. The previous appendix discusses these different formula in more detail during its 'results and conclusions' section.

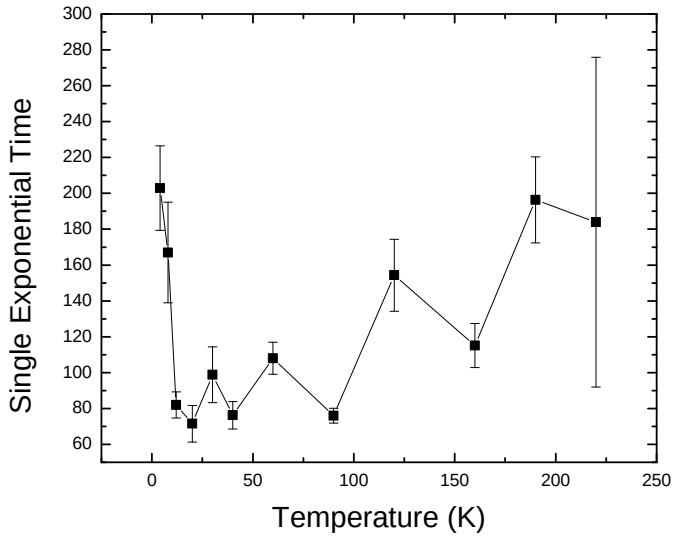

Figure B.1 Temperature dependence of spin lifetimes for 10^{17} cm^{-2} electron irradiated 4H-SiC fitted using the single-exponential regression formula.

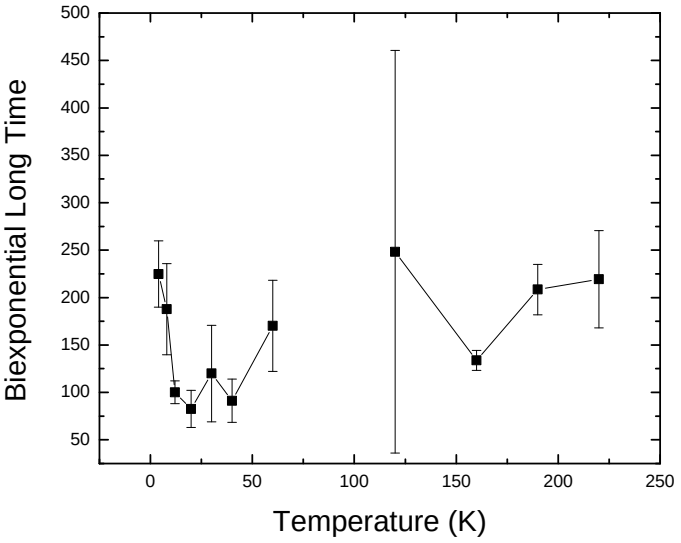

Figure B.2 Temperature dependence of spin lifetimes for 10^{17} cm^{-2} electron irradiated 4H-SiC fitted using the bi-exponential regression formula for τ_{long}. Missing points represent temperatures where data could not be fit with this type of formula. Notice the characterstic dependence similar to the results of Appendix A.

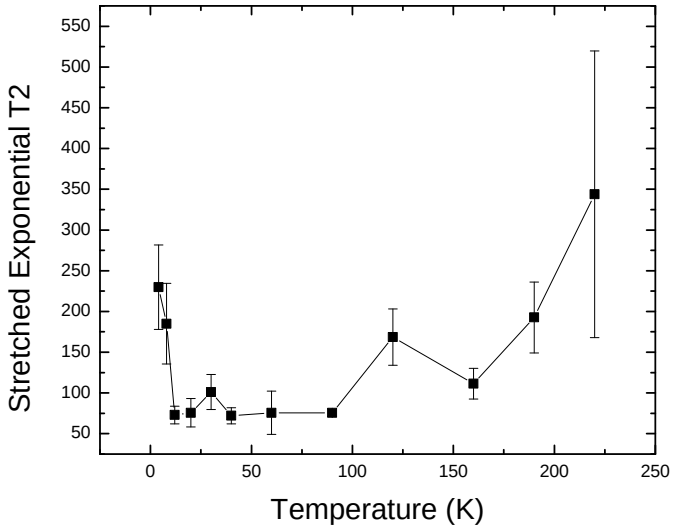

Figure B.3 Temperature dependence of spin lifetimes for 10^{17} cm^{-2} electron irradiated 4H-SiC fitted using the stretched-exponential regression formula.

Appendix C

Optical Studies of Cadmium Telluride

Thin film photovoltaics are a promising candidate in the search for cheap, efficient solar cells. In particular, cadmium telluride is one of the most widely-used materials for this application because of its leading dollar-per-watt ratio and high efficiency of around 22.3%. As part of an ongoing project, I have included the photoluminescence spectrum for a sample of CdTe given to us by Dr. Mike Scarpulla of the University of Utah. The spectrum is shown at 17.5 K (figure C.1) and room temperature (figure C.2). Note that this is only a preliminary sample of CdTe — future characterizations of CdTe will occur using a specially deposited CdTe film which has also been given to us by Dr. Mike Scarpulla.

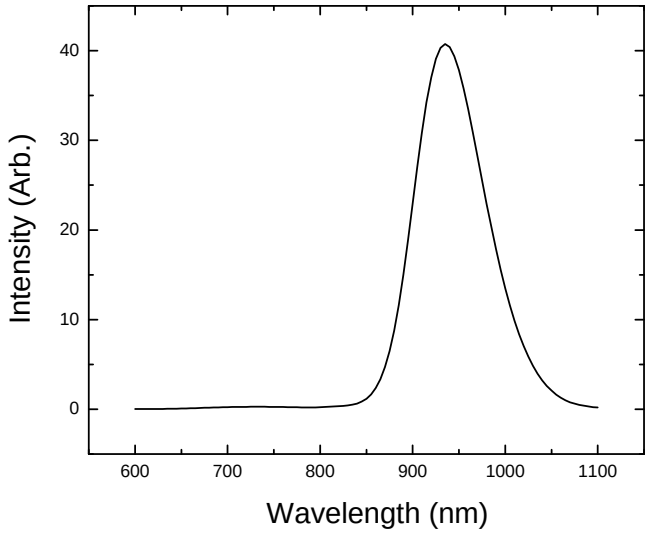

Figure C.1 Photoluminescence spectrum vs wavelength for CdTe taken at 17.5 K using a silicon detector with laser at 400 nm.

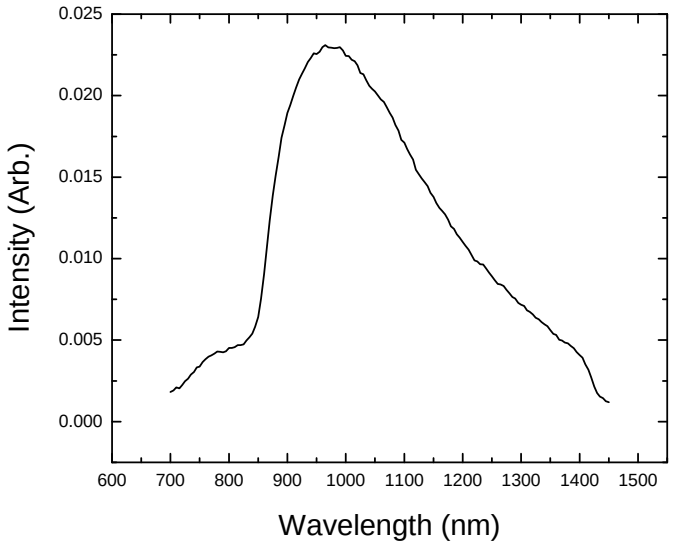

Figure C.2 Photoluminescence spectrum vs wavelength for CdTe taken at room temperature using a germanium detector with laser at 400 nm.

Bibliography

[1] H. Kobayashi, "Correlation between inter-spin interaction and molecular dynamics of organic radicals in organic 1D nanochannels," In *AIP Conference Proceedings*, 1702 (2015).

[2] N. Bar-Gill, L. M. Pham, A. Jarmola, D. Budker, and R. L. Walsworth, "Solid-state electronic spin coherence time approaching one second," Nature Communications **4,** 1–6 (2013).

[3] C. H. Bennett and D. P. Divincenzo, "Quantum information and computation," Nature **404,** 247–255 (2000).

[4] P. W. Shor, "Polynomial-time algorithms for prime factorization and discrete logarithms on a quantum computer," SIAM Review **41,** 303–332 (1999).

[5] G. V. Astakhov, D. Simin, V. Dyakonov, B. V. Yavkin, S. B. Orlinskii, I. I. Proskuryakov, A. N. Anisimov, V. A. Soltamov, and P. G. Baranov, "Spin Centres in SiC for Quantum Technologies," Applied Magnetic Resonance **47,** 793–812 (2016).

[6] M. Stavola, *Identification of defects in semiconductors* (Academic Press, San Diego, 1998).

[7] W. E. Carlos, N. Y. Garces, E. R. Glaser, and M. A. Fanton, "Annealing of multivacancy defects in 4H-SiC," Physical Review B - Condensed Matter and Materials Physics **74,** 235201 (2006).

[8] K. G. Miller, "Electron Spin Echo and Coherence Times in Silicon Carbide Defects,", Senior thesis, Brigham Young University Department of Physics and Astronomy, Provo, 2015.

[9] J. S. Embley, "Electron Spin Coherence in Silicon Vacancy Defects of Proton-irradiated Silicon Carbide,", Senior thesis, Brigham Young University Department of Physics and Astronomy, Provo, 2016.

[10] J. S. Embley, J. S. Colton, K. G. Miller, M. A. Morris, M. Meehan, S. L. Crossen, B. D. Weaver, E. R. Glaser, and S. G. Carter, "Electron spin coherence of silicon vacancies in proton-irradiated 4H-SiC," Phys. Rev. B **95,** 045206 (2017).

[11] S. G. Carter, O. O. Soykal, P. Dev, S. E. Economou, and E. R. Glaser, "Spin coherence and echo modulation of the silicon vacancy in 4H-SiC at room temperature," Physical Review B - Condensed Matter and Materials Physics **92,** 161202 (2015).

[12] S. G. Carter, E. R. Glaser, and B. D. Weaver, "Room Temperature Optically-Detected Magnetic Resonance of Silicon Vacancies in SiC,".

[13] S. Stoll and A. Schweiger, "EasySpin, a comprehensive software package for spectral simulation and analysis in EPR," Journal of Magnetic Resonance **178,** 42–55 (2006).

[14] C. P. Poole, *The theory of magnetic resonance* (Wiley-Interscience, New York, 1972), pp. 4–7.

[15] S. Stoll and R. D. Britt, "General and efficient simulation of pulse EPR spectra," Physical Chemistry Chemical Physics **11,** 6614–6625 (2009).

[16] S. Stoll, *CW-EPR Spectral Simulations: Solid State*, Vol. 563 of *Methods in Enzymology* (2015).

[17] J. E. Stehr, S. L. Chen, S. Filippov, M. Devika, N. K. Reddy, C. W. Tu, W. M. Chen, and I. A. Buyanova, "Defect properties of ZnO nanowires revealed from an optically detected magnetic resonance study," Nanotechnology **24,** 015701 (2013).

[18] E. Srman, N. T. Son, W. M. Chen, O. Kordina, C. Hallin, and E. Janzn, "Silicon vacancy related defect in 4H and 6H SiC," Physical Review B - Condensed Matter and Materials Physics **61,** 2613–2620 (2000).

[19] P. G. Baranov, A. P. Bundakova, A. A. Soltamova, S. B. Orlinskii, I. V. Borovykh, R. Zondervan, R. Verberk, and J. Schmidt, "Silicon vacancy in SiC as a promising quantum system for single-defect and single-photon spectroscopy," Physical Review B - Condensed Matter and Materials Physics **83,** 125203 (2011).

Index

cadmium telluride (CdTe), 34, 48, 49

EasySpin, 10–13, 16–23
electron paramagnetic resonance (EPR), ii, 3–5, 7, 9–12, 14–21, 23, 26, 28, 30, 33–35
electron spin resonance (ESR), ii, 3–5, 7, 9–12, 14–21, 23, 26, 28, 30, 33–35

lattice-defects, ii, 3, 7, 9, 11, 19–21, 26, 30

optically detected magnetic resonance (ODMR), i, ii, 3, 8–12, 26–29, 31, 33–36

quantum computing, ii, 3, 5–7

silicon carbide (4H SiC), ii, 8–11, 21–24, 26, 34, 36, 45
spin Hamiltonian, 12, 14–16, 18, 19, 21, 30, 35
    hyperfine contribution, 15
    spin-orbit contribution, 15
    spin-spin contribution, 15
    Zeeman contribution, 15